Journal of Marine Research, 42, 395–430, 1984

Equatorial beams

by Julian P. McCreary, Jr.[1]

ABSTRACT

A linear stratified model is used to study the response of the equatorial ocean to forcing by the wind at periods from one month to one year. Solutions are represented as double sums of vertical modes (designated by the index n) and of the various types of waves associated with each mode (designated by the index ℓ). Waves associated with a considerable number of vertical modes contribute to the solutions. They superpose in such a way that energy and phase propagate vertically as well as horizontally.

It is useful to isolate the individual contributions of various pieces of the complete solution. One way to do this isolates the response of individual vertical modes (that is, specifies a value for n, but carries out the summation over ℓ). Pieces of the solution defined in this way tend to focus energy at specific points on the equator. These focal points, however, are not at all visible in the complete solution. Another way isolates the response due to waves of a particular type (that is, fixes a value of ℓ, but carries out the summation over n). These pieces of the solution form well-defined beams that carry energy into the deep ocean at slopes predicted by inviscid ray theory, and they are visible in the complete solution.

Solutions for zonal winds are complicated. A Kelvin beam directly forced by the wind reflects from the eastern boundary of the ocean as a set of $\ell = 1, 3, 5, \ldots$ Rossby beams. These beams, in turn, reflect from the western boundary as Kelvin beams. All of them reflect efficiently from the ocean surface and bottom. It is the multiple reflection of these beams from basin boundaries that makes the response so complicated. The most visible beams in the solutions are the wind-driven Kelvin beam and a reflected $\ell = 1$ Rossby beam. The response is strong at frequencies of the order of 2π years^{-1} (or lower), and weakens considerably at higher frequencies.

Solutions for meridional winds are much simpler. At a frequency of 2π months^{-1} a beam of Rossby-gravity waves directly forced by the wind reflects entirely poleward along the eastern boundary as a packet of coastal Kelvin waves, since there are no Rossby waves available for this reflection. The response is strong at frequencies of the order of 2π months^{-1}, and weakens markedly at lower frequencies.

1. Introduction

Luyten and Swallow (1976) drew attention to the fact that the deep flow along the equator is remarkably complex. They report a set of velocity profiles taken in the western Indian Ocean during May and June of 1976. The currents were characterized by small vertical scales throughout the water column, and were trapped within a few degrees of the equator. In addition, all the profiles were similar, suggesting that the

1. Nova University Oceanographic Center, 8000 N. Ocean Drive, Dania, Florida, 33004, U.S.A.

predominant time scales of the deep currents were longer than one month. Deep currents have now been observed again in the Indian Ocean (Luyten *et al.*, 1980; Eriksen, 1980; Luyten, 1982), in the Atlantic Ocean (Weisberg and Horigan, 1981), and in the Pacific Ocean (Eriksen, 1981; Hayes and Powell, 1980; Hayes, 1981; Leetmaa and Spain, 1981; Lukas and Firing, 1984). Linear equatorial wave theory has been used with some success to interpret various aspects of the observations. In particular, there are several instances where the currents appear to be vertically propagating equatorial waves. At the present time there are only a few theoretical studies that are relevant to the phenomenon.

a. Theoretical background. Lighthill (1969) popularized the use of a linear, continuously stratified ocean model that has proven to be a valuable tool for studying wind-driven tropical circulation. He dropped nearly all nonlinear terms from the governing equations, retaining only the effects of the vertical advection of density by linearizing that term about a background density field. Wind stress entered the ocean as a body force spread uniformly throughout a surface fixed layer, rather than as a surface boundary condition, and the deeper ocean was inviscid. These simplifications allowed solutions to be found analytically in two different ways. One approach, used by Lighthill, represents solutions as expansions of *vertical* modes that propagate horizontally. A second approach represents them as expansions of *meridional* modes, and solves a vertical structure equation to determine how each mode propagates vertically. Philander (1978) contrasted both methods in some detail.

Several studies have considered the response of a single, vertical mode to low-frequency forcing by the wind (Schopf *et al.*, 1981; Cane and Sarachik, 1981; Cane and Moore, 1982). Equatorial Kelvin waves, generated by the wind field over the interior ocean, reflect from the eastern ocean boundary as a packet of Rossby waves. Surprisingly, energy associated with this packet does not propagate entirely westward, but approximately focusses back on the equator at discrete distances from the boundary. The complete response of a continuously stratified ocean model, however, is a superposition of solutions associated with many different vertical modes. None of the above studies carry out this superposition.

Wunsch (1977) studied the response of an equatorial ocean model that was dynamically very similar to Lighthill's. Forcing in the model was a surface distribution of vertical velocity (presumably driven by the wind), and had the form of a westward-propagating sinusoidal wave with a period of one year. The ocean basin was assumed to be infinitely deep and horizontally unbounded (although at the end of his paper Wunsch reported effects introduced by a western ocean boundary). He represented solutions as expansions of meridional modes, and solved the resulting vertical structure equation by matching the vertical velocity field associated with each mode to the specified surface distribution and by requiring each mode to exhibit upward phase propagation at depth (a radiation condition). In qualitative agreement

with the observations, solutions had a rich vertical structure that was narrowly confined to the equator.

There have been two studies using numerical models that discuss deep equatorial currents. Philander and Pacanowski (1981) forced a numerical model with zonal winds at various frequencies, and discussed the response in the deep ocean at a period of 200 days. Cox (1980) forced a similar numerical model with a realistic representation of the annual cycle of the Pacific trades. At the time of the year when the surface currents were most intense, they became unstable and began to meander with a wavelength of 1000 km and a period of 1.1 months. The region of unstable currents then acted as a forcing region for waves propagating into the deep ocean. Cox noted the presence of Rossby-gravity waves near a depth of 2000 m at a position 20° east of the forcing region. The amplitude of the meridional velocity field there was about 10 cm/sec.

b. The present approach. This paper continues the effort to relate the presence of deep equatorial currents to time-dependent forcing by the wind. The model ocean is essentially an extension of the Lighthill model that includes both horizontal and vertical mixing in the deep ocean, although the important dynamics of most solutions are inviscid. The ocean is forced by a patch of zonal or meridional wind that oscillates at fixed periods in a range from one month to one year. Solutions are found in both bounded and unbounded basins.

Solutions are represented as expansions of vertical modes, but it is not possible to identify the contributions of individual modes in the complete solution; in particular, equatorial focal points are not evident. Instead, equatorially trapped waves of a specific type (i.e., Kelvin waves, Rossby-gravity waves and westward-propagating Rossby waves) superpose to generate well-defined beams that carry energy into the deep ocean along ray paths, and there is vertical phase propagation across each beam. Dominant features in the solutions are consistent with some observations of deep equatorial currents.

The model is similar to the ones mentioned above. It can be regarded as an extension of the models involving a single vertical mode that includes contributions from all the modes. It can also be regarded as a generalization of the Wunsch study to a spatially limited forcing region and to a bounded ocean basin. Aspects of the present solutions also appear in the numerical solutions of Philander and Pacanowski and of Cox. Solutions are compared to those in these previous studies at several points in the paper.

2. The model ocean

In a state of no motion the model ocean has a stably stratified background density structure $\rho_b(z)$ and an associated Väisälä frequency $N_b(z)$. The model equations of motion are the familiar set that is linearized about this background state.

Under suitable conditions it is possible to represent solutions as expansions of the vertical normal modes of the system (see McCreary, 1980a, 1981a or McCreary *et al.*, 1984). These eigenfunctions, ψ_n, satisfy

$$\psi_{nz} = -\frac{N_b^2}{c_n^2}\int_{-D}^{z}\psi_n\,dz, \tag{1}$$

subject to the boundary condition

$$\frac{1}{c_n^2}\int_{-D}^{0}\psi_n\,dz = 0, \tag{2}$$

where $z = 0$, $-D$ are the depths of the ocean surface and bottom, and they are normalized so that $\psi_n(0) = 1$. It is convenient to order them so that the eigenvalues c_n decrease monotonically. The $n = 0$ eigenfunction is unique in that $c_0 = \infty$; this eigenfunction is the barotropic mode of the system. The remaining eigenfunctions form an infinite set of baroclinic modes.

The solutions for the zonal and meridional velocity fields and the pressure field are then given by

$$u = \sum_{n=1}^{N} u_n\psi_n, \qquad v = \sum_{n=1}^{N} v_n\psi_n, \qquad p = \sum_{n=1}^{N} p_n\psi_n, \tag{3}$$

where the expansion coefficients are functions only of x, y and t. It is easy to verify that the barotropic response is dominated by the baroclinic response obtained here, and so that mode is not included in the expansions (3). In addition, the sums over the infinite number of baroclinic modes are necessarily truncated at a finite value, N. Solutions converge rapidly enough with n that N need not be too large.

The equations governing the expansion coefficients are

$$\begin{aligned}
&(\partial_t + A/c_n^2)u_n - fv_n + p_{nx} = F_n,\\
&(\partial_t + A/c_n^2)v_n + fu_n + p_{ny} = G_n + \nu_h v_{nxx},\\
&(\partial_t + A/c_n^2)p_n/c_n^2 + u_{nx} + v_{ny} = 0.
\end{aligned} \tag{4}$$

The forcing of each mode is

$$F_n = \tau^x\Big/\int_{-D}^{0}\psi_n^2\,dz, \qquad G_n = \tau^y\Big/\int_{-D}^{0}\psi_n^2\,dz, \tag{5}$$

where τ^x and τ^y are the zonal and meridional components of the surface wind stress. The equatorial β-plane is adopted throughout, so that the Coriolis parameter is given by $f = \beta y$. Coefficients of vertical eddy viscosity and diffusivity are

$$\nu = \kappa = A/N_b^2, \tag{6}$$

resulting in the terms proportional to A/c_n^2. Horizontal mixing has the simple form

$\nu_h \nu_{nxx}$, in order that solutions can be represented as expansions of Hermite functions, as in (10).

Neither vertical nor horizontal mixing are significantly involved in the dynamics of the solutions found here. For most of the solutions there is no vertical mixing at all in the deep ocean (the solutions of Figures 10 and 11 are the sole exceptions). Horizontal mixing only acts to damp short–wavelength Rossby waves that reflect from the western ocean boundary, and has virtually no effect on the radiation field in the interior ocean.

Solutions are found for bounded, as well as unbounded, oceans. When boundaries exist they are vertical barriers located at the positions $x = x_0, x_1$, and there are no northern or southern boundaries. No-slip conditions are adopted at these barriers, so that basin boundary conditions are

$$u_n = v_n = 0 \quad \text{at} \quad x = x_0, x_1. \tag{7}$$

3. The solution

In this paper solutions to Eqs. (4) are found when the wind stress fields have the separable form

$$\tau^x = \tau^y = \tau_0 X(x) Y(y) e^{-i\sigma t}. \tag{8}$$

The coupling coefficients are then given by

$$\begin{aligned} F_n = G_n &= \tau_0 X(x) Y(y) e^{-i\sigma t} \Big/ \int_{-D}^{0} \psi_n^2 \, dz \\ &\equiv \tau_{0n} X(x) Y(y) e^{-i\sigma t}, \end{aligned} \tag{9}$$

where τ_{0n} is defined in the obvious manner. Here $X(x)$ and $Y(y)$ are arbitrary functions, in which $Y(y)$ weakens away from the equator, and $X(x)$ is nonzero only in a region of finite extent; hence, the model is forced by a patch of wind confined to the ocean interior.

The method of solution is essentially the same as that in McCreary (1980a, 1981a), although the algebra involved is somewhat more complicated due to the presence of horizontal mixing. For this reason, details of the derivation are not presented here. (A more detailed description of the derivation is available from the author on request.)

a. The unbounded solution. Most quantities in the following should be labelled with the subscript n (the exceptions are f, σ, X, Y and β). For notational simplicity, this subscript is subsequently deleted unless confusion might result from its absence.

Because $f = \beta y$, and because horizontal mixing has such a simple form, solutions can be expressed as expansions of Hermite functions, $\phi_\ell(\eta)$, where $\eta = (\beta/c)^{1/2} y$. The

solutions are

$$u_n = \sum_{\ell=1}^{L} u_\ell \phi_\ell, \qquad v_n = \sum_{\ell=1}^{L} v_\ell \phi_\ell, \qquad p_n = \sum_{\ell=1}^{L} p_\ell \phi_\ell, \tag{10}$$

where the expansion coefficients are only functions of x and σ. Just as in the sum over vertical modes, in principle, an infinite number of Hermite functions contribute to the sums (10). In practice, the upper limit must be truncated at a finite value, L. For realistic choices of $Y(y)$, solutions converge rapidly enough with ℓ so that L need not be too large.

For purely zonal winds, v_ℓ is

$$v_\ell(x) = i \sum_{j=1}^{4} P_j^\ell \int_{L_j}^{x} \exp\left[-ik_j^\ell x\right] X dx \exp\left[ik_j^\ell x - i\sigma t\right] \tag{11}$$

where k_j^ℓ is one of the four roots of the quartic equation

$$\frac{\nu_h}{i\omega} k^4 - \left(1 - \frac{i\omega\nu_h}{c^2}\right) k^2 - \frac{\beta}{\omega} k - \left[\alpha_0^2(2\ell + 1) - \frac{\omega^2}{c^2}\right] = 0, \tag{12}$$

and

$$P_j^\ell = \frac{i\omega}{\nu_h} \tau_{0n} \alpha_0 \frac{(1/c)[\eta Y]_\ell + (k_j^\ell/\omega)[Y_\eta]_\ell}{(k_j^\ell - k_{j'}^\ell)(k_j^\ell - k_{j''}^\ell)(k_j^\ell - k_{j'''}^\ell)} \tag{13}$$

with j, j', j'' and j''' all having different values. The expressions $[\eta Y]_\ell$ and $[Y_\eta]_\ell$ are the Hermite expansion coefficients of ηY and Y_η, respectively, $\omega = \sigma + i A/c^2$, and $\alpha_0 = (\beta/c)^{1/2}$. The lower limits on the integrals are chosen to satisfy appropriate radiation conditions [see the discussion of Eqs. (18)].

Again for zonal winds, u_ℓ is

$$\begin{aligned} u_\ell(x) &= \frac{1}{\sqrt{2}}(\ell + 1)^{1/2} R + \frac{1}{\sqrt{2}} \ell^{1/2} S + \{\delta_{\ell 0} T\} \\ &= -\frac{1}{\sqrt{2}} \alpha_0 (\ell + 1)^{1/2} \sum_{j=1}^{4} \frac{P_j^{\ell+1}}{k_j^{\ell+1} + \omega/c} \left[\int_{L_j}^{x} \exp\left[-ik_j^{\ell+1} x\right] X dx\right] \exp\left[ik_j^{\ell+1} x - i\sigma t\right] \\ &+ \frac{1}{\sqrt{2}} \alpha_0 \ell^{1/2} \sum_{j=1}^{4} \frac{P_j^{\ell-1}}{k_j^{\ell-1} - \omega/c} \left[\int_{L_j}^{x} \exp\left[-ik_j^{\ell-1} x\right] X dx\right] \exp\left[ik_j^{\ell-1} x - i\sigma t\right] \\ &+ \left\{\delta_{\ell 0} \frac{\tau_{0n}}{2c} Y_0 \left[\int_{L_3}^{x} e^{-i(\omega/c)x} X dx\right] e^{i(\omega/c)x - i\sigma t}\right\}, \end{aligned} \tag{14}$$

where $\delta_{\ell 0}$ is the Kronecker δ, and R, S and T are defined in the obvious manner. The corresponding expression for p_ℓ is

$$p_\ell(x) = c\left[-\frac{1}{\sqrt{2}}(\ell + 1)^{1/2} R + \frac{1}{\sqrt{2}} \ell^{1/2} S + \{\delta_{\ell 0} T\}\right]. \tag{15}$$

The solution for purely meridional winds is the same as that for zonal winds except that

$$P_j^{\ell} = \frac{\tau_{0n}}{\nu_h} \frac{(k_j^{\ell})^2 - \omega^2/c^2}{(k_j^{\ell} - k_f^{\ell})(k_j^{\ell} - k_{f'}^{\ell})(k_j^{\ell} - k_{f''}^{\ell})} Y_{\ell}, \tag{16}$$

and the terms in curly brackets are not present in Eqs. (14) and (15). Y_{ℓ} is the Hermite expansion of $Y(\eta)$.

b. Equatorial waves. Let k be any of the five quantities k_j or ω/c. Then, each term in (11), (14) and (15) has the form

$$\left\{ C_n \int_{L_j}^{x} e^{-ikx} X \, dx \right\} e^{ikx - i\sigma t}. \tag{17}$$

This expression describes a wave with wavenumber k, and amplitude given by the expression in curly brackets. The wave with wavenumber ω/c is an equatorially trapped Kelvin wave that is damped toward the east by vertical mixing, and the four waves with wavenumbers k_j^{ℓ} satisfy the quartic dispersion relation, (12).

When horizontal mixing is weak (as it is here) the roots of (12) separate into two distinct types. Two of them still exist when $\nu_h \to 0$. In this limit (12) reduces to the familiar quadratic dispersion relation for equatorially trapped Rossby and gravity waves, and it is therefore appropriate to refer to these two waves as Rossby or gravity waves. The two roots, labelled here k_1^{ℓ} and k_3^{ℓ}, correspond to waves with westward and eastward group velocities, respectively. They are damped both by vertical and horizontal mixing in the direction of their group velocity. The other two roots, labelled here k_2^{ℓ} and k_4^{ℓ}, decay rapidly to the west and east, respectively, with an e-folding scale of the order of 100 km. These highly damped waves are important only in boundary layers at the edges of the wind patch and at basin boundaries.

Because the amplitude in (17) is proportional to an integral of X, rather than to X itself, the amplitude is not necessarily zero outside the wind forced region. The choice of lower limit in these integrals thus governs whether radiation appears to the east, the west, or on both sides of the wind patch. Waves with eastward (westward) group velocity, or equivalently waves that decay eastward (westward) can only appear east (west) of the patch. The choices

$$L_1 = L_2 = +\infty, \qquad L_3 = L_4 = -\infty, \tag{18}$$

satisfy these requirements.

As we shall see, two types of waves that can be significantly excited by the wind are equatorially trapped Kelvin waves and Rossby-gravity waves (the waves that correspond to the indices $\ell = 0$, $j = 3$). Kelvin waves appear only in the last terms of (14) and (15), and so are generated only by zonal winds. Rossby-gravity waves can couple very efficiently to meridional winds. According to (13), they can also be generated by

zonal winds, but only by a component that is antisymmetric about the equator. Since the antisymmetric component is typically weak, Rossby-gravity waves do not couple efficiently to zonal winds.

c. Boundary effects. The unbounded solution (10) does not satisfy the constraints (7). It is necessary to add to it packets of free waves excited at ocean boundaries. Moore (1968) showed how to choose the amplitudes of these waves to ensure that $u_n = 0$ at meridional barriers, and his method has been used extensively by others [see for example, Anderson and Rowlands (1976), Cane and Sarachik (1977), McCreary (1980a, 1981a)]. The present approach is an extension of Moore's method.

Waves generated at western boundaries, designated by a prime, must have either eastward group velocities or decay to the east. These waves are

$$u'_\ell = \sum_{j=3}^{4} A_j^\ell \left[\phi_{\ell+1} - \frac{a_j^\ell}{b_j^\ell}\left(\frac{\ell}{\ell+1}\right)^{1/2}\phi_{\ell-1}\right] \exp\left[ik_j^\ell(x - x_0)\right],$$

$$v'_\ell = \frac{i}{c\alpha_0} \sum_{j=3}^{4} \frac{a_j^\ell}{\frac{1}{\sqrt{2}}(\ell+1)^{1/2}} A_j^\ell \phi_\ell \exp\left[ik_j^\ell(x - x_0)\right],$$

$$p'_\ell = c \sum_{j=3}^{4} A_j^\ell \left[\phi_{\ell+1} + \frac{a_j^\ell}{b_j^\ell}\left(\frac{\ell}{\ell+1}\right)^{1/2}\phi_{\ell-1}\right] \exp\left[ik_j^\ell(x - x_0)\right], \tag{19a}$$

where $\ell = 0, 1, 2, \ldots, a_j^\ell = ck_j^\ell - \omega$, $b_j^\ell = ck_j^\ell + \omega$, and A_3^ℓ and A_4^ℓ are, as yet, arbitrary amplitudes. An additional eastward propagating wave, labelled the $\ell = -1$, $j = 3$ wave, is the equatorially trapped Kelvin wave,

$$u'_{-1} = A_3^{-1}\phi_0 \, e^{i(\omega/c)(x-x_0)}, \; p'_{-1} = cu'_{-1}, \; v'_{-1} = 0, \tag{19b}$$

but there is no $\ell = -1$ damped wave.

Waves generated at eastern boundaries, designated by a double prime, must have westward group velocities. The appropriate waves are

$$u''_\ell = \sum_{j=1}^{2} A_j^\ell \left[\frac{b_j^\ell}{a_j^\ell}\left(\frac{\ell+1}{\ell}\right)^{1/2}\phi_{\ell+1} - \phi_{\ell-1}\right] \exp\left[ik_j^\ell(x - x_1)\right]$$

$$v''_\ell = \frac{i}{c\alpha_0} \sum_{j=1}^{2} \frac{b_j^\ell}{\frac{1}{\sqrt{2}}\ell^{1/2}} A_j^\ell \phi_\ell \exp\left[ik_j^\ell(x - x_1)\right],$$

$$p''_\ell = c \sum_{j=1}^{2} A_j^\ell \left[\frac{b_j^\ell}{a_j^\ell}\left(\frac{\ell+1}{\ell}\right)^{1/2}\phi_{\ell+1} + \phi_{\ell-1}\right] \exp\left[ik_j^\ell(x - x_1)\right], \tag{20a}$$

where $\ell = 1, 2, 3, \ldots$, and A_1^ℓ and A_2^ℓ are arbitrary amplitudes. When $\ell = 0$ an

additional westward decaying wave is

$$u_0'' = A_2^0 \frac{b_2^0}{a_2^0} \frac{\phi_1}{\sqrt{2}} \exp\,[ik_2^0(x - x_1)], \qquad p_0'' = cu_0'',$$

$$v_0'' = \frac{i}{c\alpha_0} b_2^0 A_2^0 \phi_0 \exp\,[ik_2^0(x - x_1)], \tag{20b}$$

but the $\ell = 0$ Rossby wave does not exist.

At a western ocean boundary A_3^ℓ and A_4^ℓ are chosen to cancel all components of zonal flow proportional to $\phi_{\ell+1}$ and all components of meridional flow proportional to ϕ_ℓ. For $\ell \geq 0$ this choice results in two equations for A_3^ℓ and A_4^ℓ that involve the amplitudes $A_3^{\ell+2}$, $A_4^{\ell+2}$, A_1^ℓ and $A_1^{\ell+2}$, and also the forcing terms $u_{\ell+1}(x_0)$ and $v_\ell(x_0)$ from (14) and (11). For $\ell = -1$, there is only a single equation for A_3^{-1} since there is no $\ell = -1$ damped wave. Similarly, at an eastern ocean boundary A_1^ℓ and A_2^ℓ are fixed to cancel all components of zonal flow proportional to $\phi_{\ell-1}$ and all components of meridional flow proportional to ϕ_ℓ. For $\ell \geq 1$ this choice results in two equations for A_1^ℓ and A_2^ℓ that involve the amplitudes $A_1^{\ell-2}$, $A_2^{\ell-2}$, A_3^ℓ and $A_3^{\ell-2}$ as well as $u_{\ell-1}(x_1)$ and $v_\ell(x_1)$. For $\ell = 0$ there is only a single equation for A_2^0, since the $\ell = 0$ Rossby wave does not exist.

In principle, the number of boundary waves needed is infinite. In practice, only a finite number, L, are used. It is possible to eliminate the coefficients A_2^ℓ and A_4^ℓ from equation pairs. The resulting set of equations forms a system of $2L + 2$ equations in the $2L + 2$ unknowns, $A_3^{-1}, \ldots, A_3^L, A_1^1, \ldots, A_1^L$. They can be written down in the form of a highly banded matrix equation, which can be efficiently solved on a computer. It is easy to modify this approach to find the boundary response in an ocean with only a single ocean boundary.

4. Dynamics

The radiation field in the equatorial ocean is a complex superposition of many different equatorially trapped waves. The three parts of this section discuss important properties of this radiation field. The first part points out that at the low frequencies of interest here waves associated with a large number of baroclinic modes are strongly excited by the wind. The second part shows that these waves necessarily superpose to carry energy vertically as well as horizontally along ray paths. Finally, the third part defines pieces of the complete solution that exhibit either equatorial focal points or equatorial beams.

a. The importance of high-order modes. Recall that the amplitude of a particular wave is given by the expression in curly brackets in (17), and so depends both on C_n and the value of the integral. A measure of the amplitude of the integral in the far field is the absolute value of the integral taken across the entire wind patch, that is, the absolute value of the Fourier transform of the wind, $|\tilde{X}(k)|$. This subsection discusses

how each of these factors depends on n. As we shall see, it is $|\tilde{X}(k)|$ rather than C_n that primarily determines which vertical modes appear in the solution.

For all waves in the model C_n is proportional to the coupling coefficient τ_{0n}. If the background density state has a strong near-surface pycnocline, like the curved profile in Figure 2, then τ_{0n} decreases rapidly with n. This property suggests, and has often been used to argue, that only low-order modes will significantly contribute to the solution. C_n, however, usually depends on c as well as τ_{0n}, and for this reason can be a slowly varying function of n. For example, according to (14), C_n is proportional to τ_{0n}/c for the u-field associated with a Kelvin wave. For the linear profile in Figure 2, τ_{0n}/c actually increases with n for the first ten modes or so before beginning a gradual decrease, whereas for the curved profile it decreases slowly for all values of n. Thus C_n is not a very sensitive measure of wave amplitude.

There is one exception to the preceding conclusion. For the Rossby and gravity waves C_n contains the factor $[(k_j - k_{j'})\,(k_j - k_{j''})\,(k_j - k_{j'''})]^{-1}$. The amplitude of the radiation field can be significant when this factor is large, even if $|\tilde{X}(k)|$ is not large. This property occurs near resonance points, where $k_j = k_{j'}$. (Two gravity-wave resonance points are indicated by crosses in the right panel of Fig. 1). At the low frequencies of interest here gravity-wave resonances occur only for large mode numbers ($n \approx 37$ and $n \approx 61$ in Fig. 1), and small amounts of vertical mixing act to eliminate these resonances. Rossby-wave resonances occur for sufficiently large east-west wavenumbers that they are weakened considerably by the horizontal mixing in the model. Resonant excitation of Rossby and gravity waves will not be considered further in this paper.

$|\tilde{X}(k)|$ is a very sensitive measure of wave amplitude. For the $X(x)$ defined in (31)

$$|\tilde{X}(k)| = \left| \int_{-\Delta x/2}^{\Delta x/2} \cos \frac{\pi x}{\Delta x}\, e^{-ikx}\, dx \right| = \frac{2\pi}{\Delta x} \left| \frac{\cos k\Delta x/2}{\pi^2/\Delta x^2 - k^2} \right|, \tag{21}$$

so that the strongly excited waves must satisfy the inequality

$$|k| = (k_r^2 + k_i^2)^{1/2} < 2\pi/\Delta x. \tag{22}$$

Thus, only waves with wavelengths ($2\pi/k_r$) and decay scales (k_i^{-1}) longer than the width of the wind patch couple efficiently to the wind.

The two panels of Figure 1 illustrate graphically which waves in the present model satisfy (22) at periods of one year and one month. As mentioned in the last section, the waves that are present in the interior ocean are weakly affected by horizontal mixing and for most solutions found in this paper there is no vertical mixing in the deep ocean. To a good approximation, then, these waves satisfy the familiar, inviscid, disperions relations. The curves in Figure 1 show these dispersion relations for all the baroclinic modes; only the scale factors, α_0 and $\sigma_0 = \alpha_0 c$, differ for each mode. Let the values of α_0 and σ_0 correspond to those of the linear density profile in Figure 2. Then, the thin horizontal lines indicate where $\sigma = 2\pi/\text{year}$ for the $n = 1$, 5, 15, and 25 modes (left

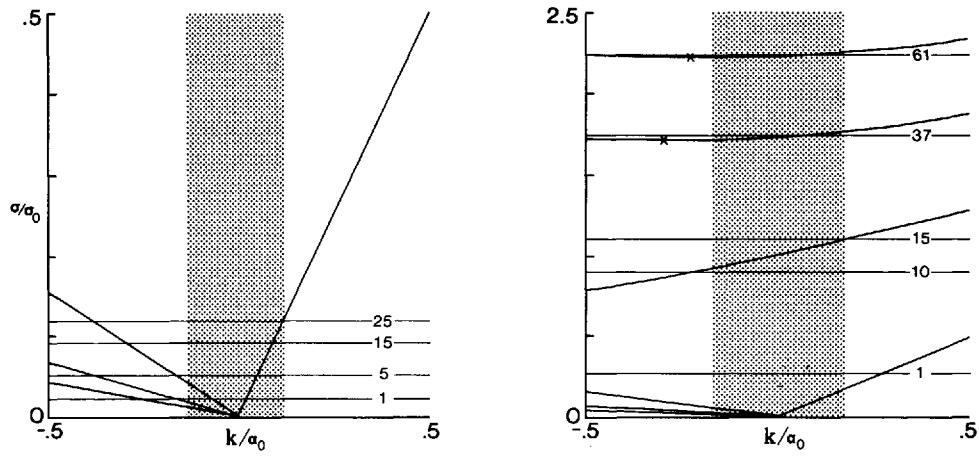

Figure 1. Dispersion curves for inviscid, equatorially trapped waves. The left panel shows the curves for the Kelvin wave and the $\ell = 1$, 3 and 5 Rossby waves; the right panel also includes the curve for the Rossby–gravity wave and the $\ell = 1$ and 2 gravity waves. Note the change in vertical scale between the two panels. The shaded areas indicate the regions, $\mathcal{A}_n$, for the $n = 20$ mode (left panel) and for the $n = 10$ mode (right panel). The thin horizontal lines indicate where $\sigma = 2\pi$ years^{-1} for the $n = 1$, 5, 15 and 25 modes (left panel), and where $\sigma = 2\pi$ months^{-1} for the $n = 1$, 10, 15, 37 and 61 modes (right panel). The crosses indicate resonance points for the gravity waves.

panel), and where $\sigma = 2\pi/\text{month}$ for the $n = 1$, 10, 15, 37 and 61 modes (right panel). The intersections of the *nth* line with the dispersion curves give the wavenumbers of the possible waves associated with the *nth* mode.

For each mode inequality (22) defines in Figure 1 a different region, $\mathcal{A}_n$, given by $|k/\alpha_0| < 2\pi/(\alpha_0 \Delta x)$. Values of $2\pi/(\alpha_0 \Delta x)$ are .53, .24, .17, .14, .12, and .11 for the $n = 1$, 5, 10, 15, 20 and 25 modes, respectively, and the shaded areas in the figure illustrate the regions $\mathcal{A}_{20}$ (left panel) and $\mathcal{A}_{10}$ (right panel). A graphical interpretation of requirement (22) is that only if the *nth* line intersects a dispersion curve inside the region $\mathcal{A}_n$ will the wave corresponding to that intersection by significantly excited by the wind.

The left panel of Figure 1 indicates that at the annual frequency the above criterion is satisfied for all the Kelvin waves associated with the $n < 20$ modes (only the intersection of the $n = 25$ frequency line with the Kelvin-wave dispersion curve lies clearly outside $\mathcal{A}_{25}$). On the other hand, the criterion is satisfied for a much smaller number of Rossby waves. For example, the $n = 5$ frequency line does intersect the dispersion curve for the $\ell = 1$ Rossby wave inside $\mathcal{A}_5$ but does not do so for the $\ell = 3$ or $\ell = 5$ Rossby waves; for the $n = 10$ mode none of the Rossby wave intersections lie inside the shaded region, $\mathcal{A}_{10}$. Thus, a wind patch oscillating at the annual period efficiently generates Kelvin waves associated with a large number of vertical modes (provided that the wind is zonal), but excites Rossby waves to a lesser degree.

The right panel of Figure 1 indicates that at the monthly frequency only the gravest mode Kelvin waves, and no Rossby waves at all, are significantly excited by the wind. On the other hand, Rossby-gravity waves associated with the modes $10 \lesssim n \lesssim 15$, the $\ell = 1$ gravity wave for the $n \approx 37$ modes, and the $\ell = 2$ gravity wave for the $n \approx 61$ modes all couple efficiently to the wind. The gravity waves, however, occur for such large mode numbers that even a small amount of vertical mixing virtually eliminates them, and so gravity waves are not an important part of any of the solutions found in this paper (see the discussion of Fig. 11). Thus, a wind patch oscillating at a period of one month efficiently generates only Rossby-gravity waves (provided that the wind is meridional).

b. Vertical propagation. It is not obvious that waves associated with several baroclinic modes must superpose to exhibit vertical propagation of phase and energy. One method of demonstrating this property is to avoid entirely the expansion into vertical modes by representing solutions as expansions of meridional modes (Philander, 1978). In contrast, the method discussed in the following modifies the solution found in Section 3 by representing solutions as expansions of a continuous, rather than discrete, set of vertical modes.

According to WKB theory (Bender and Orszag, 1978), approximate solutions to (1) and (2) have the form

$$\psi_n(z) = A(z) \cos\left(\int^z m dz\right), \tag{23}$$

where $A(z) = N_b^{1/2}$, $m = N_b/c$ is a local vertical wavenumber, and $c^{-1} = n\pi \int_{-D}^{0} N_b dz \equiv \xi$. Let $b \equiv N_b/N_{bz}$ measure the vertical scale of $N_b(z)$. Then the WKB solution is valid to order $(mb)^{-2}$. Since the cosine in (23) can be written as the sum of two complex exponentials, it is apparent that each vertical mode consists of one wave with phase propagating upward and another with phase propagating downward.

To determine where energy associated with superpositions of these waves goes, it is useful to write the solution in an integral form that does not involve sums over a discrete set of vertical modes. Suppose that the depth of the ocean increases, and that N_b approaches a constant value in the deep ocean. Then, since $\int_{-D}^{0} N_b dz$ increases with D, the allowed values of ξ become ever more densely packed, and in the limit $D \to \infty$ they become continuously distributed (Morse and Feshbach, 1953). The mathematical development in the previous section can be easily modified to describe this situation. The important difference is that in (3) the discrete sums over n are replaced by integrals over the continuous variable ξ. (A finite-depth ocean bottom can be included in this new formulation by using the method of images. In that case, both the discrete and integral representations produce identical solutions.) It is now possible to utilize the method of stationary phase (or similar technique) to determine where the solution

is large in the far field (Lighthill, 1978). It follows that waves of a specific type (that is, for a given value of ℓ) superpose to carry energy along ray paths.

The ray paths are determined by the dispersion relations of the various waves. With the replacement $c = N_b/m$ the dispersion relation for inviscid, equatorially trapped Kelvin waves becomes

$$\sigma = kN_b/m. \tag{24}$$

Similarly, according to (12), the dispersion relation for inviscid, Rossby-gravity waves becomes

$$k = \sigma m/N_b - \beta/\sigma \tag{25}$$

and that for low-frequency, low-wavenumber, inviscid Rossby waves [for which the k^2 and ω^2 terms in (12) are negligible] becomes

$$\sigma = -k\frac{N_b/m}{2\ell + 1} \tag{26}$$

for $\ell = 1, 2, 3, \ldots$. Let the zonal and vertical components of group velocity be c_{gx} and c_{gz}. The slope of ray paths is $\tan\theta_e = c_{gz}/c_{gx} = \pm\sigma_m/\sigma_k$, where the upper (lower) sign holds for waves with upward (downward) phase propagation. Values of $\tan\theta_e$ obtained from (24), (25), and (26) are $\mp\sigma/N_b$, $\mp\sigma/N_b$, and $\pm(2\ell + 1)\,\sigma/N_b$, respectively. Thus, when phase propagates upward, energy propagates downward to the east for Kelvin and Rossby-gravity waves and downward to the west for Rossby waves. The slopes are quite small. With $N_b = .0045$ sec^{-1} (the value corresponding to the linear density distribution of Fig. 2) and at the annual frequency, $\sigma/N_b = 45$ m/1000 km; at the monthly frequency, $\sigma/N_b = 530$ m/1000 km.

An oscillating wind patch in the ocean interior excites waves with both upward and downward phase propagation. Wave packets with upward phase propagation carry energy directly away from the wind patch down into the deep ocean. Wave packets with downward phase propagation, however, carry energy toward the ocean surface. They subsequently reflect from the surface as a packet of waves that carry energy downward. Consequently, the only waves that appear in the deep ocean (outside the region of direct influence by the wind and before they reflect from the ocean bottom) are waves with upward phase propagation.

By definition, lines of constant phase in the x-z plane have the slope $\tan\theta_p = -c_z/c_x = \mp k/m$. For Kelvin waves and the Rossby waves that satisfy (26) it is easy to verify that $\theta_p = \theta_e$. Thus, for these waves lines of constant phase are everywhere parallel to the direction of energy propagation. A very different property holds for Rossby-gravity waves. Because the Rossby-gravity waves that are significantly excited by the wind patch are large-scale ($k < 2\pi/\Delta x \ll \beta/\sigma$), k is negligible in (25). For these large-scale

waves, then,

$$m = N_b \beta / \sigma^2. \tag{27}$$

It also follows that $\theta_p \approx 0$, so that lines of constant phase are essentially horizontal.

When there is a sharp pycnocline, so that b becomes a small number, the WKB approximation is not valid for low-order vertical modes. The effect is that some energy can reflect off the pycnocline (Philander, 1978), rather than propagate along ray paths through it. Surprisingly, for the pycnocline structure used here ray theory appears to work very well (see the discussion of Figs. 8 and 11). Rothstein (private communication) is currently studying the reflection of energy from various pycnoclines in detail.

c. Focal points and beams. Let q be any of the fields u, v or p. Then the complete solution can be summarized as

$$q = \sum_{n=1}^{N} \left[\sum_{\ell=0}^{L} q_\ell \phi_\ell(\eta) + \sum_{\ell=-1}^{L} q'_\ell + \sum_{\ell=1}^{L} q''_\ell \right] \psi_n(z), \tag{28}$$

where the q_ℓ are defined in (11), (14) and (15), the q'_ℓ in (19) and the q''_ℓ in (20). Eq. (28) is complicated, and it is useful to separate out the individual contributions of less complex pieces of (28). Since the solution is a double sum over n and ℓ, this separation can proceed conveniently in two very different ways.

One way considers the response of an individual baroclinic mode, that is, specifies a value of n and carries out the summation over all values of ℓ. As discussed in the introduction, several studies have already considered the response of a single mode to low-frequency forcing, and have found that Rossby waves reflected from the eastern boundary tend to focus energy back to the equator at specific points. Currents are large in the vicinity of these focal points, but are small elsewhere. One might expect that near these focal points a particular baroclinic mode will stand out above all the others in the complete solution. As we shall see, however, such a dominance is not at all apparent in the solutions found in the next section.

The other way specifies the value of ℓ and carries out the summation over all values of n. For example, the contribution of $\ell = \lambda$ Rossby waves generated at the eastern boundary is

$$q_\lambda = \sum_{n=1}^{N} q''_\lambda \psi_n(z), \tag{29}$$

and the contribution of Kelvin waves generated at the western boundary is

$$q_{-1} = \sum_{n=1}^{N} q'_{-1} \psi_n(z). \tag{30}$$

Pieces of the solution calculated in this manner form well-defined beams of energy

that exhibit all the properties discussed in the previous subsection, and they are visible in the complete solution (see the discussion in Section 5c). They are, in fact, analogous to the vertically propagating meridional modes in Wunsch's model.

5. Results

The model was used to study the response of the ocean to a zonal and meridional wind patch with a simple, but geophysically relevant, structure. The wind field has the form (8) with $\tau_0 = .125$ dyne/cm^2,

$$X(x) = \begin{cases} \cos(\pi x/\Delta x), & |x| \le \Delta x/2 \\ 0, & |x| > \Delta x/2 \end{cases} \tag{31}$$

and

$$Y(y) = (1 + y^2/\Delta y^2)\, e^{-y^2/\Delta y^2}, \tag{32}$$

where $\Delta x = 5000$ km and $\Delta y = 1000$ km. For $y < \Delta y$, $Y(y)$ is virtually constant, and none of the results discussed below depend on the structure of $Y(y)$. The shaded region of Figure 3 indicates the extent of the wind patch, and the thin line its zonal profile. For zonal winds almost always $\sigma = 2\pi$ years^{-1}, the sole exceptions being the solutions shown in Figure 7. For meridional winds usually $\sigma = 2\pi$ months^{-1}, the exceptions being the solutions in Figure 10.

Figure 2 shows the two profiles of background density structure, $\rho_b(z)$, assumed here. Both profiles have a surface mixed layer of thickness $H = 75$ m. Unless stated otherwise, the choice of density profile is always the one that varies linearly with depth beneath the mixed layer. The linear profile has the advantage that ray paths are straight lines and therefore it is easier to interpret the response in the deep ocean. The curved profile is described by

$$\rho_b(z) = \begin{cases} \rho_0, & z \ge -H \\ \rho_0 + \Delta\rho_1[1 - e^{-(z+H)/b_1}] \\ \quad + \Delta\rho_2[1 - e^{-(z+H)/b_2}], & z < -H, \end{cases} \tag{33}$$

where $b_1 = 200$ m, $b_2 = 1000$ m, $\rho_0 = 1$ gm/cm^3, $\Delta\rho_1 = .003$ gm/cm^3, $\Delta\rho_2 = .002$ gm/cm^3. This profile has a strong near-surface pycnocline, typical of the density structure in the central tropical Pacific.

Unless stated otherwise, the model ocean has both eastern and western boundaries at $x_0 = -5000$ km and $x_1 = 5000$ km. The positions of the boundaries are indicated in Figure 3. The depth of the ocean is $D = 2500$ m. The value of horizontal eddy viscosity is $\nu_h = 10^7$ cm^2/sec. Usually $A = 0$ so that there is no vertical mixing beneath the surface mixed layer, the exceptions being the solutions in Figures 10 and 11. It is necessary to choose sufficiently large values of N and L in the sums of (3) and (10).

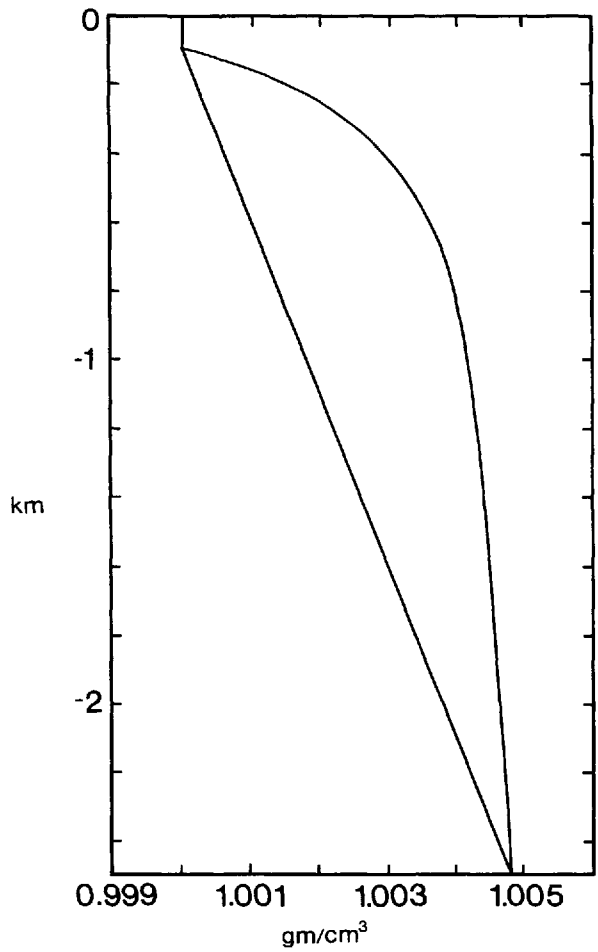

Figure 2. Profiles of background density structure, $\rho_b(z)$. One profile has a constant gradient below a surface mixed layer 75 m thick. The other profile has a strong near-surface pycnocline typical of the tropical oceans, and is described by Eq. (33). Most results correspond to the linear profile.

The choices $N = 50$ and $L = 75$ adopted here ensure that solutions are well converged.

a. Solutions for zonal winds. Three velocity sections describe the three-dimensional flow field. Figure 3 shows the positions of these sections relative to the equator and to ocean boundaries. Figures 4a and 4b show zonal and meridional circulation patterns corresponding to Sections 1–3 of Figure 3 at time $t = 0$. There is considerable energy in the deep ocean. Considering the small amplitude of the wind, the strength of the response is surprising.

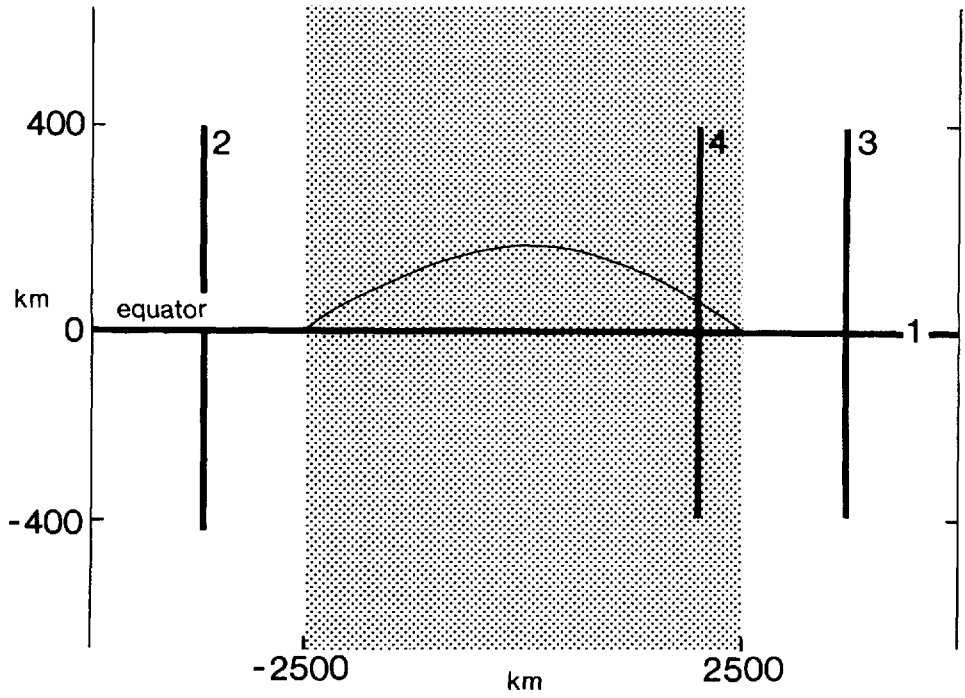

Figure 3. A schematic diagram showing the locations of Sections 1–4, the position of ocean boundaries, and the structure of the wind field. The shaded region indicates the extent of the wind field, and the thin line its zonal profile. Its meridional profile is very nearly latitude-independent. The wind stress varies sinusoidally reaching an eastward or northward maximum at $t = 0$, and has a maximum amplitude of .125 dyn/cm^2 in the center of the ocean basin. The structure of the wind is described more precisely in Eqs. (31) and (32).

The flow field in Figure 4 is complicated. The most prominent feature in the equatorial section is the presence of a band of energy that descends from a depth of 250 m at the eastern boundary to a depth of 1700 m at the western boundary. There are also two regions where energy appears to be bottom trapped: near $x = -1500$ km and near $x = 2500$ km. The meridional sections illustrate that currents are highly trapped to the equator. Along Section 2 the strongest currents occur between 1300 m and 2000 m, and are to a large degree associated with the band of energy evident in Figure 4a. Along Section 3 the flow field has a remarkable honeycomb structure, with more cells appearing deeper in the water column.

The response of each of the baroclinic modes that contributes to Figure 4 has distinct focal points at the expected positions along the equator. Curiously, these focal points are not at all evident in Figure 4a, where the contributions from all the modes are summed. For example, there are no regions where a single vertical mode visually dominates the solution. This fact suggests that it is not particularly useful to separate the solution into a set of contributions from individual baroclinic modes. On the other

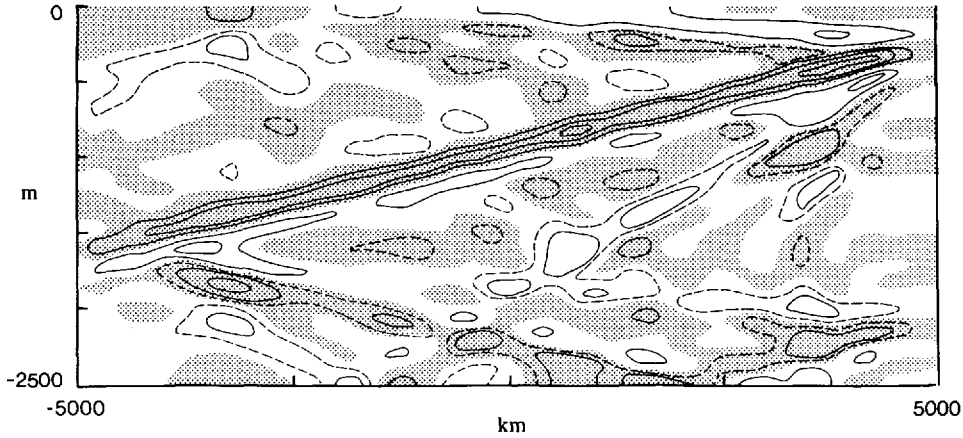

Figure 4a. A section of zonal velocity along the equator, when the ocean is forced by a patch of zonal wind that oscillates at the annual frequency. The contour interval is 20 cm/sec, there is no zero contour line, and shaded regions indicate westward (negative) flow. Dashed contour lines are ±10 cm/sec, and are included only if they help to identify prominent features of the flow field. The section is taken at $t = 0$, the time of maximum eastward wind. There is considerable energy in the deep ocean.

hand, vertical phase propagation occurs virtually everywhere along the equator. There are regions where phase propagates upward, and also many places where phase propagates downward. This property suggests that it is useful to interpret the solutions as being a superposition of equatorial beams, and the rest of this section pursues this interpretation.

i. The effect of boundaries. How important are ocean boundaries for the generation of energy in the deep ocean? Figure 5 shows three sections of zonal velocity that are comparable to Figure 4a except that the ocean is unbounded, has only a western boundary, and has only an eastern boundary in the upper, middle and lower panels, respectively.

Without ocean boundaries there are no strong currents anywhere in the deep ocean. Energy goes into the deep ocean primarily along two beams that propagate east and west of the wind patch with specific slopes. To the east of the wind patch the beam has the slope $-\sigma/N_b$, and so is composed of Kelvin waves. To the west of the wind patch the beam has the slope $3\sigma/N_b$, and so is composed of $\ell = 1$ Rossby waves. Phase propagates upward and there is a 2π-phase shift across each beam. The presence of a western boundary only slightly modifies the unbounded response. The $\ell = 1$ Rossby beam reflects from the western boundary as a Kelvin beam that is visible at a depth of about 1000 m in the middle panel, but there is very little energy in this reflected beam. The presence of the eastern boundary has a dramatic effect on the unbounded response. The Kelvin beam reflects from the eastern boundary as a collection of beams of Rossby

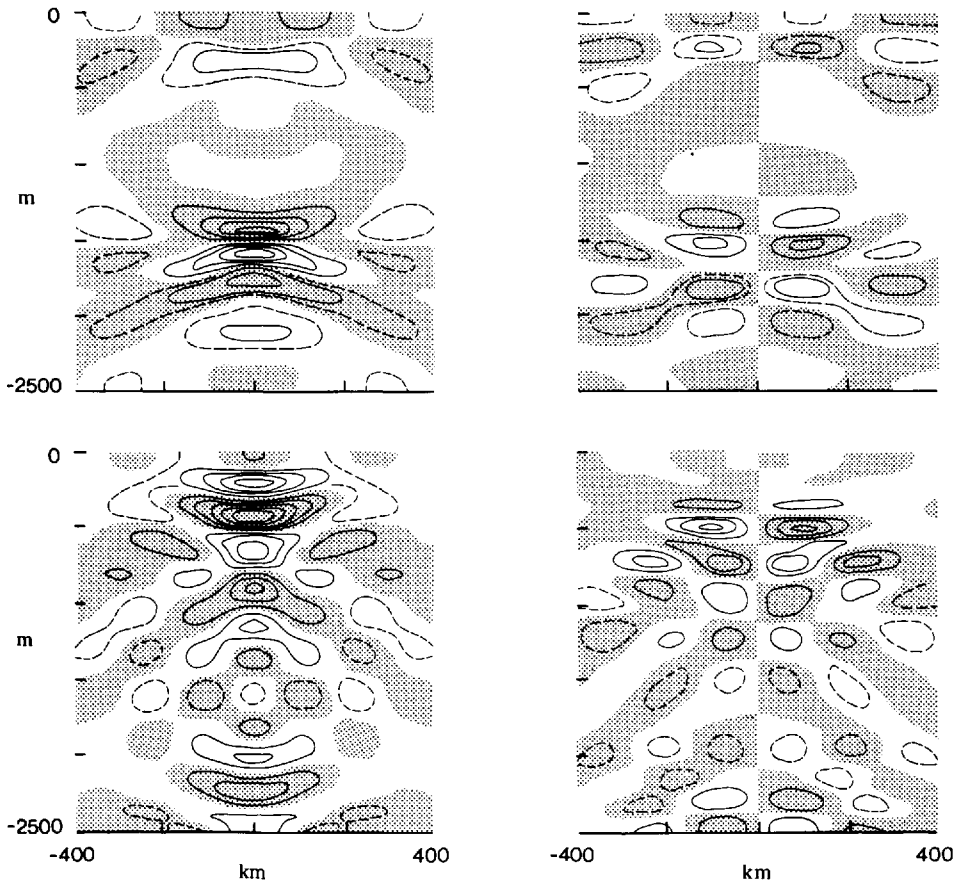

Figure 4b. As in Figure 4a, except showing sections of zonal and meridional velocity along Section 2 (upper panels) and Section 3 (lower panels) of Figure 3. The shaded regions indicate westward or southward (negative) flow. The contour interval for zonal velocity (left panels) is 10 cm/sec, and the dashed contours are ±5 cm/sec. The contour interval for meridional velocity (right panels) is 2.5 cm/sec and the dashed contours are ±1.25 cm/sec. The currents have a distinct cellular structure that is trapped to the equator; this property is especially evident along Section 3.

waves that propagate energy into the deep ocean. Note that the prominent band of energy in Figure 4a is evident in the lower panel. Clearly an eastern ocean boundary is required in order to get significant radiation into the deep ocean.

In apparent contrast to the present study, the Wunsch (1977) model produced a great deal of energy in the deep ocean even though the ocean basin was unbounded. The important difference between the two models is that the forcing in Wunsch's model was not limited zonally. The analog of Wunsch's solution in the present model occurs when $X(x)$ in (31) is replaced by $X(x) = \cos(\pi x/\Delta x)$ for all x. So, the flow field

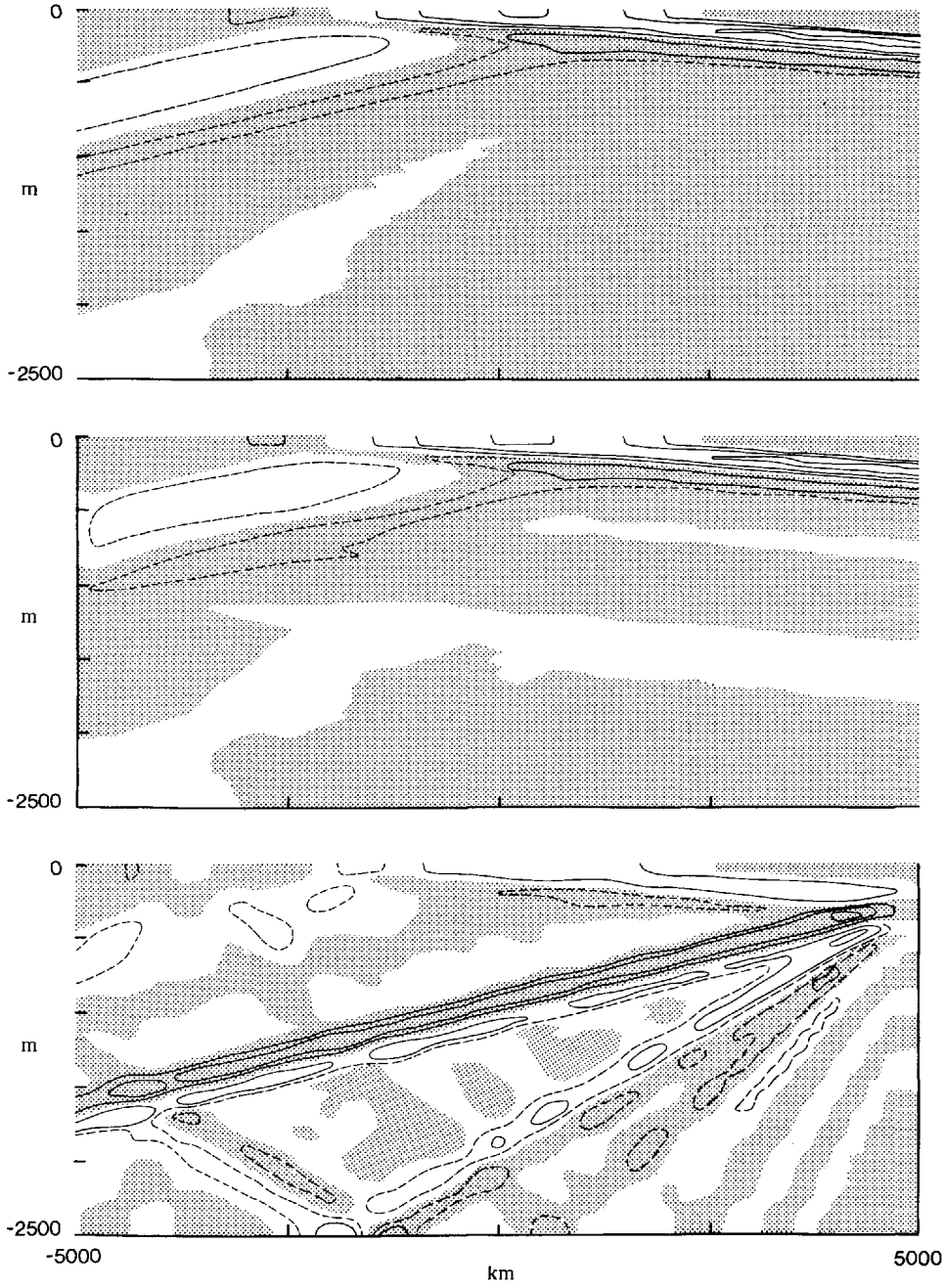

Figure 5. As in Figure 4a, except that the ocean basin is unbounded in the upper panel, lacks an eastern boundary in the middle panel, and lacks a western boundary in the lower panel. The contour interval in the upper and middle panels is 10 cm/sec, and the dashed contours are ± 5 cm/sec. The contour interval in the lower panel is 20 cm/sec, and the dashed contour lines are ± 10 cm/sec. A strong beam of Kelvin waves, generated by the wind, is evident in all the panels. It propagates into the eastern ocean with the slope $-\sigma/N_b$. Only when the ocean has an eastern boundary does significant energy get into the deep ocean.

in the upper panel of Figure 5, $u(x,z)$ say, results from only one piece of this sinusoidal forcing, the piece contained in the region $|x| < \Delta x/2$. The analog solution is therefore $\sum_{n=-\infty}^{\infty} (-1)^n u(x - n\Delta x, z)$. In this solution, then, radiation will appear in the deep ocean near $x = 0$, but it will have been produced by a remote part of the forcing (for which $|n| \gg 1$). The same conclusion holds for the Wunsch solution.

ii. Equatorial beams. Figure 6 shows the contribution of various boundary-generated waves to the flow field of Figure 4. The three panels of Figure 6a show the contributions of the $\ell = 1$, 3, and 5 Rossby waves, as defined in (29), that are generated at the eastern boundary. Figure 6b shows the contributions of Kelvin waves, as defined in (30), that are generated at the western boundary. Figure 6c shows meridional sections of each of these contributions along Section 3 of Figure 3.

In each case the waves superpose to form well-defined beams of energy that propagate along the equator at the slopes predicted by ray theory, that is, at the slopes $\pm\sigma/N_b$ for the Kelvin beam, and $\pm 3\sigma/N_b$, $\pm 7\sigma/N_b$, $\pm 11\sigma/N_b$ for the $\ell = 1$, 3 and 5 Rossby beams, respectively. Phase lines are everywhere parallel to beam paths. Phase propagates upward across Rossby (Kelvin) beams that slope downward to the west (east), whereas phase propagates downward across upward-sloping beams, and there is a 2π-phase shift across each of the beams. Beams readily reflect from the ocean bottom and surface. Wherever such a reflection occurs downward and upward beams interfere to produce locally a bottom or surface trapped structure that resembles a standing wave. Phase propagates through this structure westward (eastward) for Rossby (Kelvin) beam reflections. The meridional structures of the beams have more current reversals and are less equatorially trapped as ℓ increases. This property is expected, since as ℓ increases they are composed of higher-order Hermite functions.

Figure 6 illustrates that the amplitudes of the Rossby beams decrease markedly with ℓ, so that higher-order Rossby beams ($\ell \geq 7$) contribute very little to the equatorial currents. To a good approximation, then, the flow field of Figure 4a is the superposition of the upper panel of Figure 5 with Figures 6a and 6b. With the aid of these figures it is now possible to identify the contributions of individual beams in Figure 4a. In particular, the prominent band of energy is an $\ell = 1$ Rossby beam. The two regions of bottom-trapped energy are identified as places where an $\ell = 1$ Rossby beam and an $\ell = 3$ Rossby beam reflect from the ocean bottom. Regions of downward phase propagation occur whenever a beam has reflected from the ocean bottom. Similarly, the lower left panel of Figure 4b is approximately a superposition of all the panels of Figure 6c with the near-surface Kelvin beam directly driven by the wind (see the upper panel of Fig. 5). The honeycomb structure in this panel occurs because the contributing equatorial beams all appear at different depths, with the Kelvin beam most shallow and the $\ell = 1$, 3 and 5 Rossby beams at ever increasing depths.

There are three Rossby beams evident in each of the panels of Figure 6a. They originate at the eastern boundary near the ocean surface at a depth of about 250 m, and

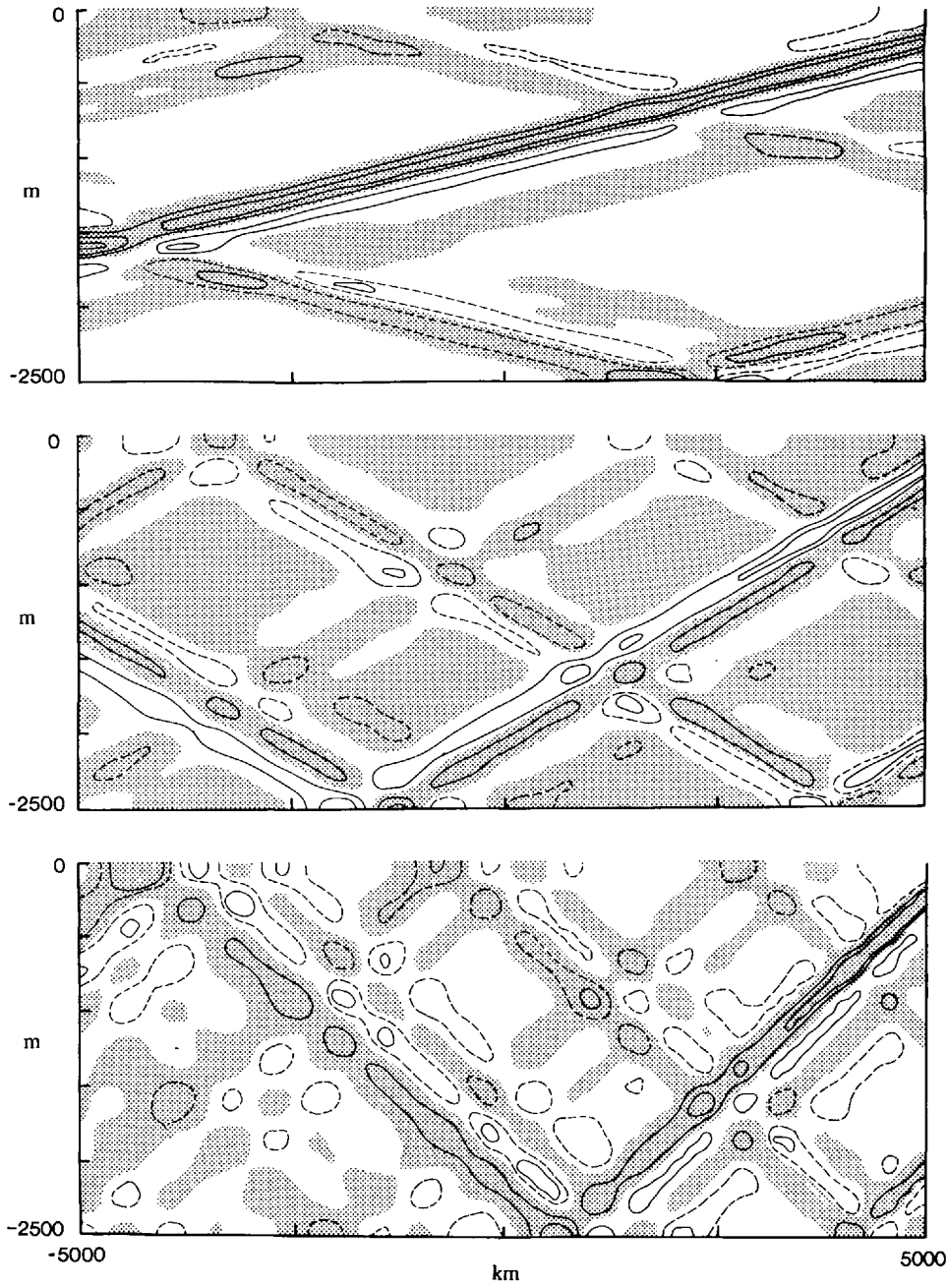

Figure 6a. As in Figure 4a, except that only the contributions of Rossby waves generated at the eastern boundary are shown. The figure shows the $\ell = 1$ Rossby waves in the upper panel, the $\ell = 3$ Rossby waves in the middle panel, and the $\ell = 5$ Rossby waves in the lower panel. The contour intervals are 20, 10 and 5 cm/sec and dashed contour lines are ± 10, ± 5, and ± 2.5 cm/sec in the upper, middle and lower panels, respectively. Beams of Rossby waves propagate from the eastern boundary with the slopes $\pm(2\ell + 1)\,\sigma/N_b$. There are three obvious sources of these beams at depths of about 250 m, 1200 m and 2200 m.

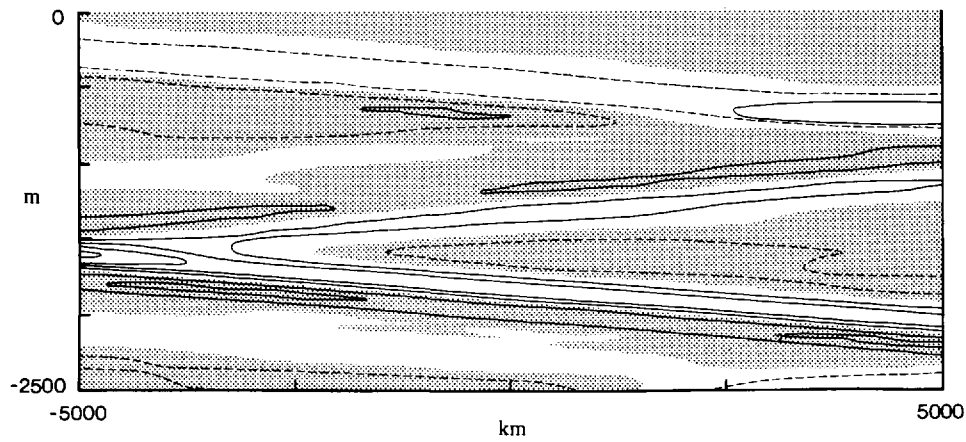

Figure 6b. As in Figure 4a, except that only the contributions of Kelvin waves generated at the western boundary are shown. The contour interval is 5 cm/sec, and the dashed contour lines are ±2.5 cm/sec. Beams of Kelvin waves propagate from the western boundary with the slopes $\pm\sigma/N_b$. The sources of the two strongest beams, one sloping downward toward the east and the other sloping upward occur at depths of 1700 m and 1500 m, respectively.

much deeper at depths of about 2200 m and 1200 m. It is convenient for the discussion in the following paragraph to label the three $\ell = 1$ Rossby beams R1, R2 and R3, respectively. There are also three Kelvin beams prominent in Figure 6b. A downward-sloping Kelvin beam originates at the western boundary near a depth of 1700, and an upward-sloping one begins at 1500 m. The third beam originates at a depth of 250 m. These beams are labelled K1, K2 and K3, respectively.

This collection of beams is the result of multiple reflections of Kelvin and $\ell = 1$ Rossby beams between ocean boundaries in the following way. The Kelvin beam directly generated by the wind (see the upper panel of Fig. 5) reflects from the eastern boundary at a depth of about 250 m predominantly as R1 (although $\ell = 3, 5, \ldots$, Rossby beams are also generated by this reflection). R1 reflects from the western boundary at a depth of 1700 m as K1. K1, in turn, reflects from the eastern boundary at a depth of 2200 m predominantly as R2. R2 reflects first from the ocean bottom and then from the western boundary at 1500 m as the Kelvin beam, K2. K2 reflects from the eastern boundary at 1000 m as R3, and R3 reflects first from the ocean surface and then from the western boundary at 250 m to generate K3.

iii. The dependence on model parameters. It is important to know how the response of the model varies with the choice of free parameters. Since ν_h does not significantly affect the deep flow, the important parameters are σ, $\rho_b(z)$ and A.

Figure 7 shows two sections of zonal velocity comparable to Figure 4a except that $\sigma = 4\pi$ years^{-1} and $\sigma = 8\pi$ years^{-1} in the upper and lower panels, respectively. In both panels it is easy to identify the wind-driven Kelvin beam and one reflected $\ell = 1$ Rossby

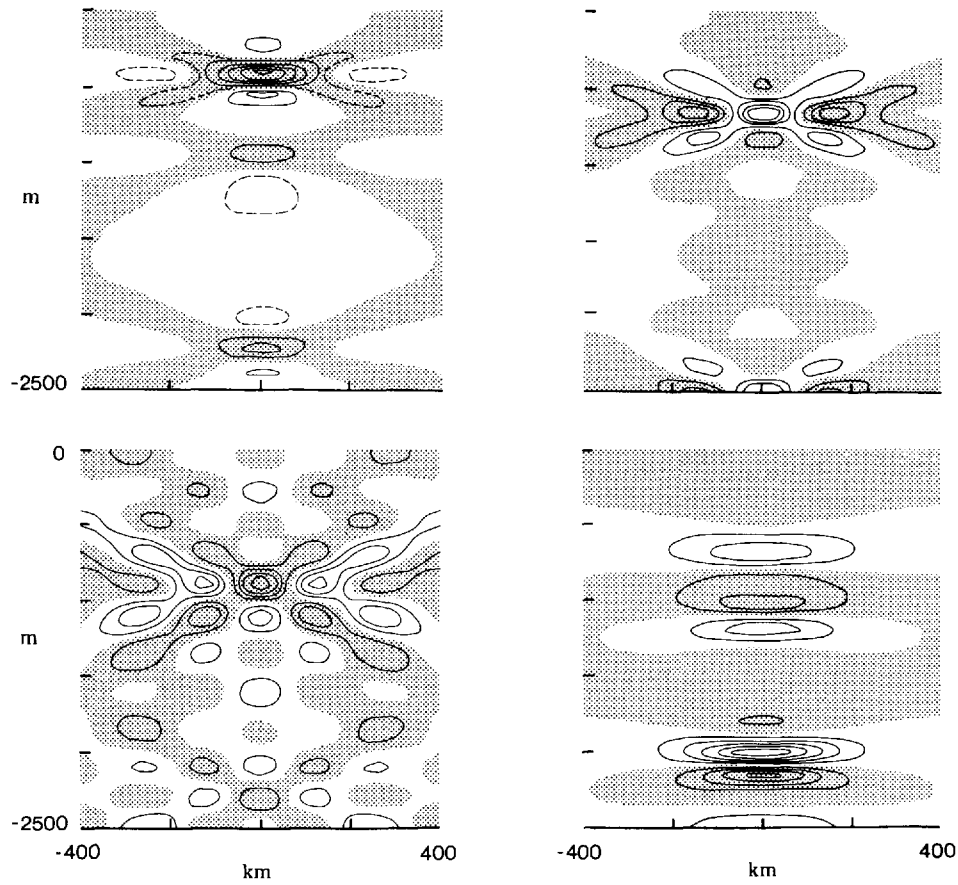

Figure 6c. Similar to Figure 4b, except that only the contributions of waves generated at ocean boundaries are shown, and the sections are all taken along Section 3 of Figure 3. The figure shows $\ell = 1$ Rossby waves in the upper left panel, $\ell = 3$ Rossby waves in the upper right panel, $\ell = 5$ Rossby waves in the lower left panel, and Kelvin waves in the lower right panel. The contour intervals are 10, 5, 2.5 and 2.5 cm/sec in the upper left, upper right, lower left and lower right panels, respectively. The meridional structures of individual beams have more current reversals as ℓ increases.

beam (equivalent to R1 in Fig. 6a), but other equatorial beams are not as readily apparent. As expected, in the upper panel beam slopes are twice as large as they are in Figure 4a, and in the lower panel they are four times as large. Note that the amplitude of the deep ocean response decreases markedly as σ increases. The reason for this decrease is that at higher frequencies fewer Kelvin waves can couple efficiently to the wind field (see the discussion in Section 4a), and so the wind-driven Kelvin beam itself is much weaker.

Figure 8 shows a section of zonal flow that is comparable to Figure 4a except that

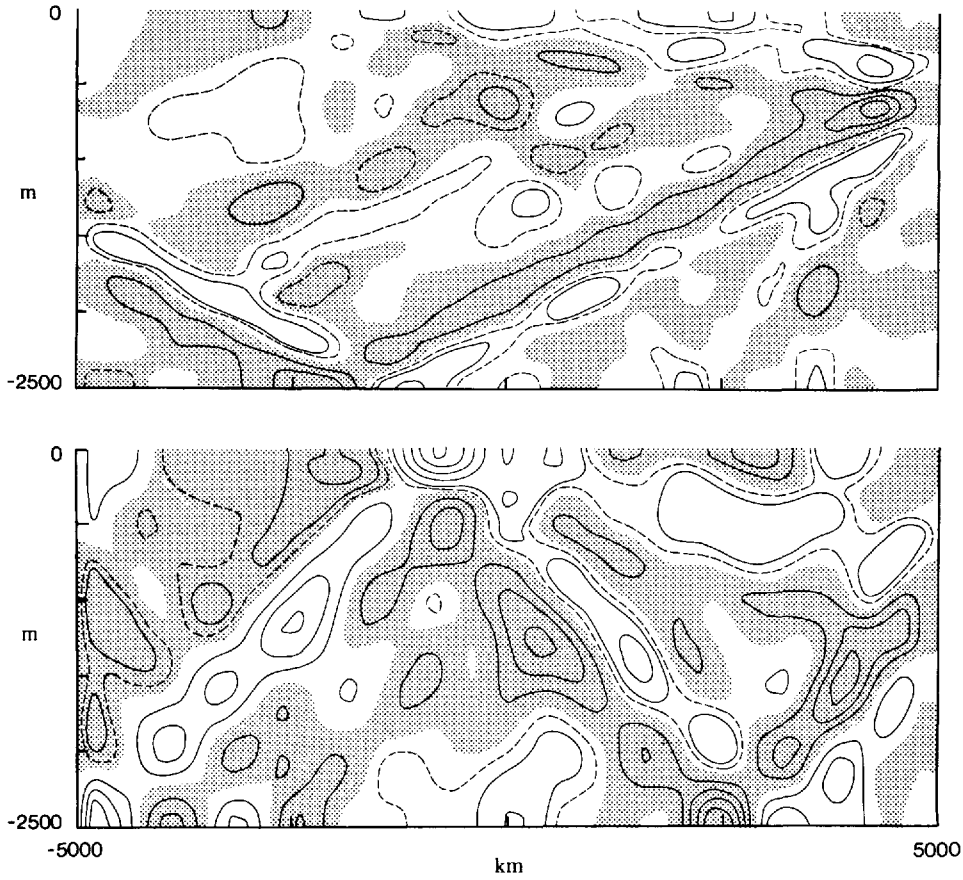

Figure 7. As in Figure 4a, except that the wind oscillates with a period of 6 months in the upper panel, and with a period of 3 months in the lower panel. The contour interval in the upper panel is 10 cm/sec, and dashed contour lines are ±5 cm/sec. The contour interval in the lower panel is 2.5 cm/sec, and dashed contour lines are ±1.25 cm/sec. The wind-driven Kelvin beam and the $\ell = 1$ Rossby beam are evident in each panel. The amplitude of the currents weakens markedly as frequency increases.

$\rho_b(z)$ is now the depth–varying profile in Figure 2. Because N_b is not constant, beam paths are no longer straight; they slope more steeply in the deep ocean where N_b is smaller. Note that the beams readily pass through the pycnocline, so that the pycnocline does not act to trap the flow field near the ocean surface. One effect of this steepening is that beams broaden considerably as they propagate into the deep ocean. Several equatorial beams are visible in the figure. Again, the wind-driven Kelvin beam and the reflected $\ell = 1$ Rossby beam (equivalent to R1) are most prominent. An $\ell = 3$ Rossby beam can also be seen leaving the eastern boundary at a depth near 200 m, reflecting from the ocean bottom near $x = 0$, and returning almost to the surface at the

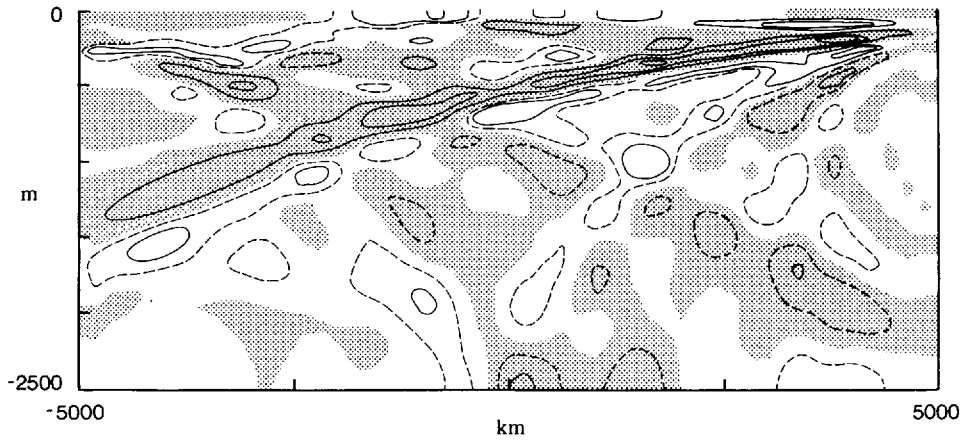

Figure 8. As in Figure 4a, except that N_b varies with depth in a realistic manner. The contour interval is 20 cm/sec, and the dashed contours are ±10 cm/sec. Beams are still evident in the flow field, but their paths are now curved. The $\ell = 1$ Rossby beam is most evident. The $\ell = 3$ Rossby beam reflects from the ocean bottom and returns near to the surface in the western ocean.

western boundary. Another $\ell = 1$ Rossby beam (equivalent to R2) leaves the eastern boundary near a depth of 2000 m, propagates upward and arrives near the surface at the western boundary. The source of this deep beam is a Kelvin beam (equivalent to K1) that leaves the western boundary near a depth of 1500 m, reflects from the ocean bottom near $x = 2000$ km, and reaches the eastern boundary near a depth of 2000 m.

Vertical mixing acts to weaken equatorial beams in their direction of propagation, and to broaden them both vertically and meridionally. This broadening occurs because waves associated with higher-order vertical modes are preferentially damped out of the beam. In spite of these effects energy still propagates along ray paths, in agreement with inviscid theory. McCreary (1980b, 1981b) showed a solution comparable to the one in Figure 4, except that A was set so that $\nu = .55$ cm^2/sec. The broadening of equatorial beams is evident in that solution. In particular, the vertical extent of the prominent $\ell = 1$ Rossby beam in the central and western ocean increases to 750–1000 m.

iv. Comparison with a numerical model. As mentioned in the introduction, Philander and Pacanowski (1981) describe the response of their model in the deep ocean when the wind stress has a period close to the semi-annual (200 days). Beneath a sharp pycnocline confined above 200 m, their initial density state was weakly stratified with a constant value of $N_b = 1.8 \times 10^{-3}$ sec^{-1}. The value of N_b for the linear profile of Figure 2 is $N_b = 4.5 \times 10^{-3}$ sec^{-1}. Thus, beam slopes in this model are about 2.5 times steeper than they are in the upper panel of Figure 7, and so have about the slope that they do in the lower panel of the figure.

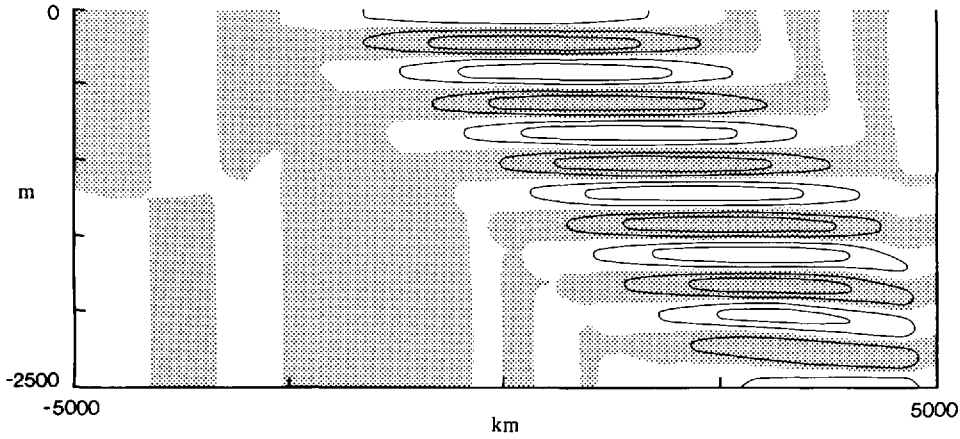

Figure 9a. As in Figure 4a, except that a patch of meridional wind oscillating at the monthly frequency forces the ocean. The shaded region indicates southward flow, and the contour interval is 5 cm/sec. A beam of Rossby-gravity waves propagates into the ocean with the slope $-\sigma/N_b$. There are no Rossby waves available to reflect this beam from the eastern boundary, and so the beam reflects entirely poleward as a beam of coastal Kelvin waves.

Their figures suggest that the deep flow in their model is similar to that developed in this one. In particular, their deep flow appears to be dominated by a wind-driven Kelvin beam and the primary, reflected $\ell = 1$ Rossby beam (equivalent to R1 in Fig. 6a). In the central ocean above 750 m and below the pycnocline the flow field exhibits upward propagation of phase (their Fig. 6), consistent with the presence of a Kelvin beam. At a position 1600 km from the eastern boundary the flow is concentrated above 1500 m and again exhibits upward phase propagation (their Fig. 16), consistent with the presence of the Kelvin beam and a reflected $\ell = 1$ Rossby beam. At a position 3200 km from the boundary, a region of deep flow (distinct from the near-surface currents) extends from a depth of 1000 m to the ocean bottom; although there is clear evidence of upward phase propagation, the vertical structure of this flow also has some characteristics of a standing wave (their Fig. 16). Bottom currents are strongest in a region 2000–4000 km from the eastern boundary, and they exhibit westward phase propagation (their Fig. 15). The meridional structure of the zonal velocity field near the bottom is strongly trapped to the equator with a single weak current reversal somewhat off the equator. All these properties are consistent with the presence of an $\ell = 1$ Rossby beam that reflects from the ocean bottom at a position centered about 3000 km from the eastern boundary.

b. Solutions for meridional winds. Figures 9a,b show zonal and meridional circulation patterns corresponding to Sections 1 and 4 of Figure 3 at time $t = 0$. A beam of energy, highly trapped to the equator, descends into the deep ocean at the slope $-\sigma/N_b$. Phase lines are not parallel to the beam path, but rather are horizontal. Finally, the vertical

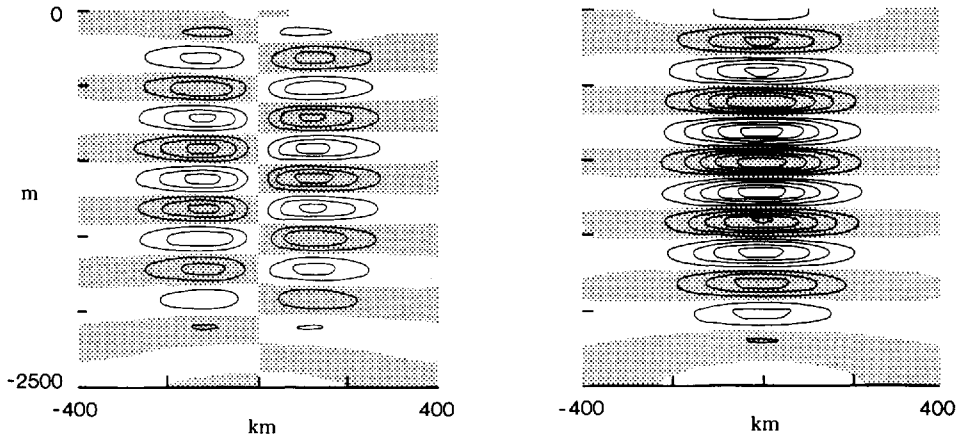

Figure 9b. As in Figure 9a, except showing sections of zonal velocity (left panel) and of meridional velocity (right panel) along Section 4 of Figure 3. The shaded regions indicate the presence of westward or southward (negative) flow, and the contour interval in both panels is 2.5 cm/sec. Currents are highly trapped to the equator.

wavelength of the beams is exactly that predicted by (27). These properties indicate that the beam is composed of Rossby-gravity waves. Considering the small amplitude of the wind, the strength of the response is again surprising.

In contrast to Figure 4, the solution of Figure 9 has a very simple structure. The complex response of Figure 4 is entirely due to the fact that at low frequencies Rossby waves reflect a considerable amount of energy back into the interior ocean. At a period of one month, however, there are no Rossby waves available for this reflection. (A graphical interpretation of this property is that none of the horizontal lines in the right panel of Figure 1 ever intersect any of the dispersion curves for $\ell > 2$ Rossby waves.) Instead, the Rossby-gravity beam reflects entirely poleward via β-plane Kelvin waves as discussed by Moore (1968) (also see McCreary, 1980a).

Figure 10 shows the model response at a somewhat lower frequency, $\sigma = 2\pi/\sqrt{2}$ months^{-1}. In the upper panel $A = 0$, so that there is no mixing in the deep ocean, whereas in the lower panel A is set so that $\nu = .25$ cm^2/sec there. Consistent with (27), the vertical wavelength of the response decreases by a factor of 2. Without vertical mixing the Rossby-gravity beam descends into the deep ocean, just as in Figure 9. With vertical mixing, however, the Rossby-gravity beam decays markedly away from the ocean surface. At even lower frequencies this decay is much more severe because the vertical wavelength decreases so rapidly with σ. As a result, the deep response of the model to this meridional wind patch at periods greater than one month is negligible.

Figure 11 shows a section of meridional flow that is comparable to that in Figure 9 except that $\rho_b(z)$ is now the depth-varying profile in Figure 2, and there is vertical mixing in the deep ocean. According to (6), since $N_b(z)$ is not constant, mixing coefficients vary with depth. Just beneath the mixed layer N_b attains a maximum

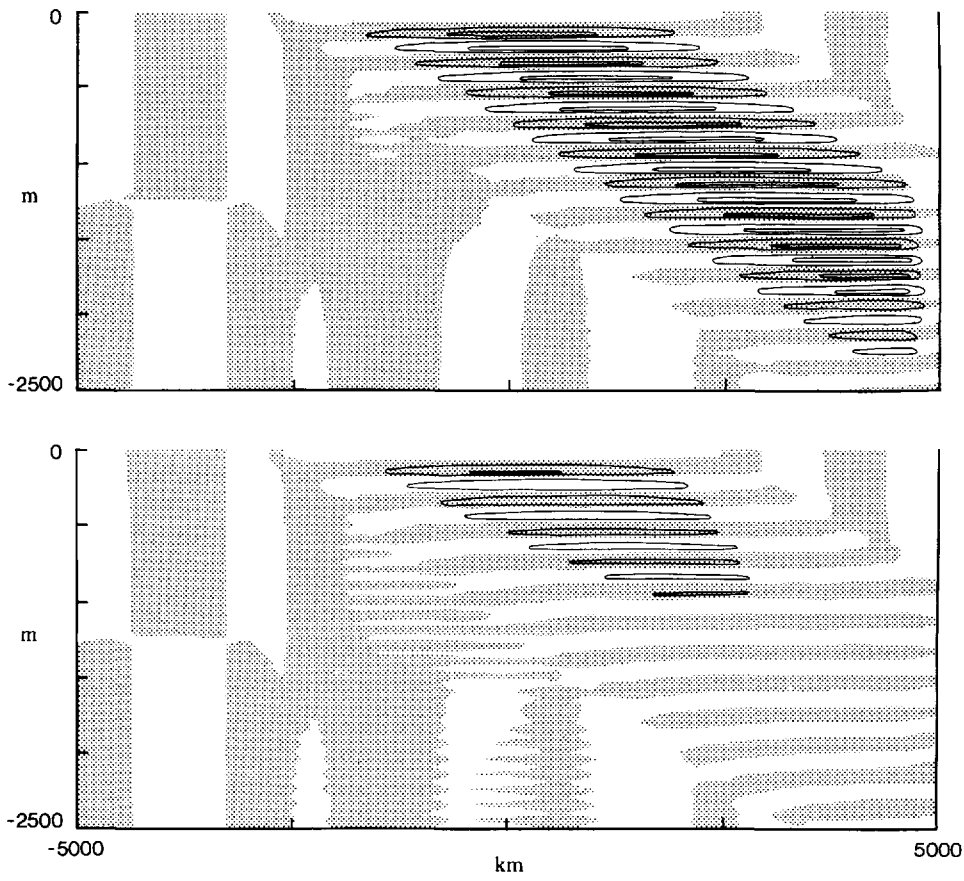

Figure 10. As in Figure 9a, except that the frequency of the wind is decreased by a factor of $\sqrt{2}$. In the upper panel there is no vertical mixing, whereas in the lower panel $\nu = .25$ cm^2/sec. The contour interval in both panels is 10 cm/sec. The vertical wavelength of the beam decreases by a factor of 2. Vertical mixing acts to weaken severely Rossby-gravity beams at lower frequencies.

value, and so ν and κ reach a minimum value, ν_{min}. A is set so that $\nu_{min} = .25$ cm^2/sec. As in Figure 8, beam paths are no longer straight, but slope more steeply in the deeper ocean, becoming nearly vertical there. As a result, the Rossby-gravity beam reflects first from the ocean bottom near $x = 3500$ km before it reflects from the eastern boundary. The radiation in the deep eastern ocean is a combination of downward and upward propagating Rossby-gravity beams and so forms a standing wave pattern with no vertical propagation.

As discussed in Section 4a gravity waves associated with very high-order vertical modes can be generated by the wind patch. For the depth-varying density profile of Figure 2, $\ell = 2$ gravity waves for the $n \approx 48$ modes couple efficiently to the wind

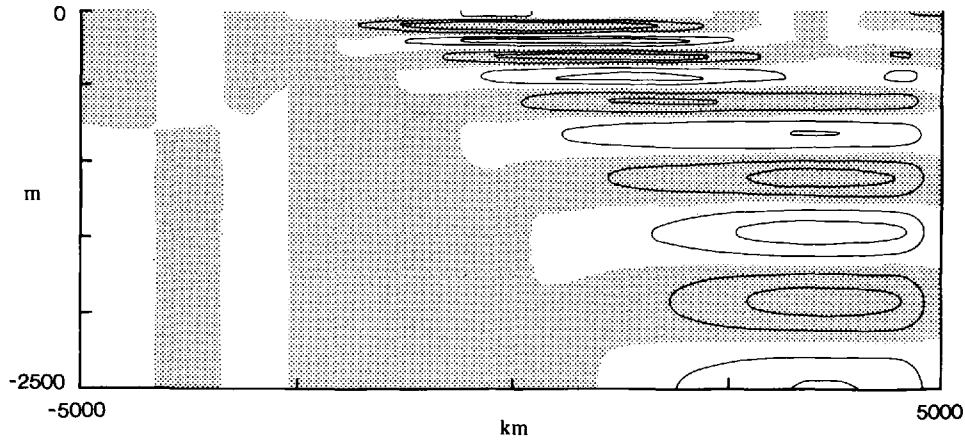

Figure 11. As in Figure 9a, except that N_b varies with depth in a more realistic manner and $\nu_{min} = .25$ cm^2/sec. The contour interval is 5 cm/sec. The Rossby-gravity beam now follows a curved path, reflects from the ocean bottom, and begins to return near the surface in the far eastern ocean. The response in the deep eastern ocean is a standing wave pattern, because it is the result of interference between downward and upward propagating beams.

(rather than for the $n \approx 61$ modes as in Fig. 10). Without vertical mixing these waves are a source of short vertical-wavelength noise that is comparable in amplitude to the Rossby-gravity beam itself. With $\nu_{min} = .25$ cm^2/sec this noise is completely eliminated, and the structure of the Rossby-gravity beam is hardly affected at all.

The Cox model generated a Rossby-gravity beam similar to the one in Figure 11. A difference between the two cases is that his surface forcing propagated westward with a specific zonal wavenumber, k_0. So, the analog of Cox's solution in the present model occurs when $X(x)$ in (31) is replaced by $X(x)e^{ik_0x}$, so that the wind has the form of an amplitude–modulated travelling wave. The Fourier transform of this wind field is peaked about $k = k_0$ rather than $k = 0$. Thus, the strongly excited Rossby-gravity waves necessarily have zonal wavenumbers near k_0. The major effect on the deep flow is that phase propagates horizontally as well as vertically; phase lines are no longer horizontal, but have a slope approximately given by $\tan \theta_p = (\sigma/N_b)k_0/(k_0 + \beta/\sigma)$. The slope of the beam is still $\tan \theta_e = -(\sigma/N_b)$. Similar properties hold for the Cox solution.

c. Comparison with observations. For zonal winds the most visible aspect of the solutions are the Kelvin beam directly generated by the wind, and the $\ell = 1$ Rossby beam excited by the reflection of the Kelvin beam at the eastern ocean boundary, as in Figure 8. For meridional winds the dominant feature is a Rossby-gravity beam, as in Figure 11. The two important characteristics of these signals are that phase propagates vertically and that energy propagates along ray paths. Is it possible to observe such signals in the real ocean? One observational difficulty is that to identify a beam in its

entirety requires a long time series of observations that extend throughout the water column and that are widely separated zonally. Another is that forcing by the wind is not generally peaked about a single frequency as assumed here, with the possible exception being the annual cycle and its harmonics. Finally, the zonal structure of the real wind does not have a form as simple as that assumed here. As a result, at the present time an observational base does not exist that can prove or disprove the existence of beam-like signals in the equatorial ocean. There are some observations, however, that are consistent with such an interpretation.

The best evidence for the existence of an $\ell = 1$ Rossby beam is that presented by Lukas and Firing (1984). Monthly hydrographic sections were taken at one-degree intervals across the equator in the central Pacific (at 150W, 153W and 158W) for a 16-month period during the NORPAX Hawaii-to Tahiti shuttle experiment. Lukas and Firing extracted the annual cycle from this data set, thereby determining the amplitude and phase of the temperature signal as a function of latitude and depth. The amplitude had two relative maxima roughly symmetric about the equator and located at a depth of 450 m near 2N and 2S. Upward phase propagation was evident in the signal from a depth of 900 m to the near-surface pycnocline (near 150 m). By extrapolating the signal deeper into the ocean they inferred that a vertical wavelength (2π-phase shift) of 2200 m was associated with the signal. Eriksen (1981) reported an annual signal in the deep equatorial zonal current somewhat farther west (at 175E); the amplitude of the signal at a depth of 1200 m and 1400 m was 5–10 cm/sec. Lukas and Firing suggested that this signal was related to the one they observed. They interpreted both to be due to the presence of an $\ell = 1$ Rossby beam, originating either at the eastern boundary (as in Fig. 8) or directly forced by the wind (as is evident in the upper panel of Fig. 5).

In a similar analysis, Lukas (1981) formed bimonthly averages of all available hydrographic data from the eastern tropical Pacific. He extracted both the annual and semiannual cycles from this data at two locations on the equator (at 82W and 92W). There was a clear upward propagation of phase in the semi-annual signal at both longitudes in a depth range from 500 m to 100 m, with an inferred vertical wavelength of about 800 m. This property is good evidence that this signal is remotely forced, and so is likely to be a combination of an incoming Kelvin beam and a reflected $\ell = 1$ Rossby beam. Upward phase propagation was not as apparent for the annual cycle.

There is indirect evidence of an annual, equatorial Kelvin beam in the Atlantic. Picaut (1983) observed upward phase propagation of the annual upwelling event in a depth range from 300 m to 50 m just off the coast of Africa at 5N near Abidjan (4W). He concluded that this signal was a beam of coastal Kelvin waves that was remotely generated by the reflection of an equatorial Kelvin beam from the coast of Africa. McCreary *et al.* (1984) modelled this reflection process in a study similar to the present one. An equatorial Kelvin beam generated by zonal winds in the western Atlantic reflected primarily not only as an $\ell = 1$ Rossby beam, but also as a beam of

coastal Kelvin waves along the coast at 5N, in good agreement with Picaut's observations.

Luyten and Roemmich (1982) discussed current records taken in the western Indian Ocean (47E–59W) from April, 1979 to June, 1980. Current meters were situated at depths of 200 m, 500 m and 750 m. In the Indian Ocean a semi-annual oscillation dominates the zonal component of the wind. The semi-annual oscillation also dominated the zonal component of the flow for all the current meters, but was absent in the meridional component. There was no detectable phase lag of this signal between instruments separated horizontally. Cross-correlation of records from instruments separated vertically, however, showed upward propagation of phase with an inferred vertical wavelength of about 2800 m. Current records from the same location but several years earlier (Luyten, 1982) showed a weak semi-annual signal at 1500 m and virtually none at greater depths. All these observations are consistent with the presence of an $\ell = 1$ Rossby beam that is confined in the upper ocean. The reflected beam in the upper panel of Figure 7 slopes rapidly into the deep ocean. It is therefore more likely that their signal is the result of an $\ell = 1$ Rossby beam that is directly generated by the wind, rather than one that has reflected from the eastern boundary.

McPhaden (1982) discussed a two-year time series of current profiles collected every week in the central Indian Ocean (73E) in a depth range from 200 m to the surface. As expected the zonal currents had a strong semi-annual component. In the surface mixed layer the flow was in-phase with the wind. Beneath the mixed layer the amplitude of the signal decreased markedly with depth. In addition, phase decreased with depth, indicating that phase propagates upward in time. These properties are consistent with the presence of a wind-driven Kelvin beam (or an $\ell = 1$ Rossby beam) just beneath the well-mixed upper layer.

Weisberg and Horigan (1981) describe current records taken in the eastern, equatorial Atlantic (4W) from June, 1976 to May, 1978. From August to December an oscillation with a period of one month appeared in the meridional component of the flow, but not in the zonal component. There was clear upward propagation of phase with a vertical wavelength of about 1000 km. Weisberg and Horigan interpreted this signal to be a beam of Rossby-gravity waves, and with the aid of the dispersion relation for these waves [Eq. (25)] estimated a horizontal wavelength of 1200 km. They concluded that their signal must be forced by unstable surface currents, as in the Cox model. The present results support this conclusion. The fact that the data are associated with a short horizontal wavelength indicates that the source is not a large-scale oscillating wind patch, as for the solution in Figure 11. If it is generated by the wind it must be due to a periodic, westward-propagating disturbance with a wavelength of 1000 km, and there is no observational evidence that such a wind field exists.

O'Neill (1982) analyzed in detail the velocity profiles first reported by Luyten and Swallow (1976). She found evidence for the presence of two Rossby-gravity waves in the

data. One of them had a period of 57 days, was associated with upward phase propagation, had a vertical wavelength of 450 m and an estimated horizontal wavelength of 730 km. The other, and more prominent one, had a period of 72 days, a vertical wavelength of 1200 m, and an estimated horizontal wavelength of 300–400 km. Remarkably, phase propagates downward for this signal indicating upward energy propagation. The origin of either of these waves is unknown.

6. Summary and discussion

A linear, continuously stratified model is forced by a patch of zonal or meridional wind that oscillates at periods from one month to one year. Solutions are represented as sums over vertical modes and also over the various types of waves associated with each mode, as in (28). Typically, the responses associated with a considerable number of vertical modes contribute to the solution. This property is a bit surprising since wave amplitudes, C_n, are proportional to τ_{0n}, and τ_{0n} typically decreases rapidly with n. However, wave amplitudes depend on c_n as well as τ_{0n}. For example, the zonal velocity field corresponding to a Kelvin wave is proportional to τ_{0n}/c_n and this quantity decreases slowly (or even increases) with n. Wave amplitudes are also determined by the Fourier transform of the wind field, $\tilde{X}(k)$, and this factor is a very sensitive measure of C_n. Essentially, all waves will be strongly excited that have wavenumbers for which $|\tilde{X}(k)|$ is large, regardless of which vertical mode they are associated with.

Because the solution is represented as a discrete sum of vertical modes, it is not obvious that energy must propagate vertically as well as horizontally. By letting the ocean bottom become infinitely deep, discrete sums are replaced by integrals. It is then possible to use various mathematical techniques (like the method of stationary phase) to determine where the solution will appear in the far field. It follows that waves of a given type propagate energy along their respective ray paths.

Pieces of the solution corresponding to a particular vertical mode [for a fixed value of n in (28)] focus energy back on the equator at distinct points. Focal points, however, are not at all visible in the complete solution. Pieces of the solution that correspond to waves of a particular type [for a fixed value of ℓ in (28), as in (29) and (30)] form well-defined beams that carry energy into the deep ocean along ray paths. There is a 2π-phase shift across each beam, and they readily reflect from basin boundaries. Beams are visible in the complete solution.

Zonal winds efficiently generate a Kelvin beam that reflects from the eastern boundary as a set of Rossby beams. The resulting flow field is very complex. There are many features having a short vertical scale. There are regions where phase propagates upward, where phase propagates downward, and also regions of apparent bottom-trapped flow. Little energy appears in the deep ocean when the basin has no eastern boundary, indicating that reflected Rossby waves play a crucial role in the dynamics of deep, low-frequency currents in the model. The model response is strongest when the wind has a period of one year, and weakens markedly at higher frequencies.

Meridional winds efficiently generate a beam of Rossby-gravity waves. At a period of one month this beam reflects entirely poleward along the eastern boundary as a packet of coastal Kelvin waves, since there are no Rossby waves available for the reflection. The resulting flow field is much simpler than that for zonal winds. Energy descends into the deep ocean with a small vertical scale, and there is upward propagation of phase. The reflection of the Rossby-gravity beam from the ocean bottom produces a standing-wave pattern.

The best evidence for the presence of beams comes from observations of vertically propagating, equatorially trapped signals. Observations discussed by Lukas (1981), McPhaden (1982) and Picaut (1983) are consistent with the presence of a wind-driven Kelvin beam. The observations of Lukas and Firing (1984) and of Luyten and Roemmich (1982) suggest the existence of an $\ell = 1$ Rossby beam. Variability in the deep ocean discussed by Weisberg and Horrigan (1981) and by O'Neill (1982) appear to be Rossby-gravity waves. Because the estimated horizontal wavelength of these waves is short, however, they cannot be generated by a large-scale oscillating wind patch, as in Figure 11.

The important result of this paper is that it provides a theoretical picture of the deep ocean currents that are generated by low-frequency winds. Although these flows can be quite complex they simplify considerably when viewed as superpositions of equatorial beams. It is hoped that the ideas discussed in this paper will facilitate the understanding of more comprehensive, numerical models of the deep, equatorial ocean. More importantly, it is hoped that the notion of equatorial beams will provide a useful way of interpreting some of the observations of deep currents.

Acknowledgments. This research was sponsored by the National Science Foundation under grant no. OCE 79-21785 through PEQUOD. The author is indebted to Joël Picaut, Roger Lukas and Dennis Moore, for many stimulating and enlightening discussions during the course of this study. Pijush Kundu and David Anderson suggested several improvements of an earlier version of this paper.

REFERENCES

Anderson, D. L. T. and P. B. Rowlands. 1976. The role of inertia-gravity and planetary waves in the response of a tropical ocean to the incidence of an equatorial Kelvin wave on a meridional boundary. J. Mar. Res., *34,* 295–312.

Bender, C. M. and S. A. Orszag. 1978. Advanced Mathematical Methods for Scientists and Engineers, McGraw-Hill, New York, 593 pp.

Cane, M. A. and D. W. Moore. 1982. A note on low-frequency equatorial basin modes. J. Phys. Oceanogr., *11,* 1578–1584.

Cane, M. A. and E. S. Sarachik. 1977. Forced baroclinic ocean motions: II. The linear equatorial bounded case. J. Mar. Res., *35,* 395–432.

—— 1981. The response of a linear baroclinic equatorial ocean to periodic forcing. J. Mar. Res., *39,* 651–693.

Cox, M. D. 1980. Generation and decay of 30-day waves in a numerical model of the Pacific. J. Phys. Oceanogr., *10,* 1168–1186.

Eriksen, C. C. 1980. Evidence for a continuous spectrum of equatorial waves in the Indian Ocean. J. Geophys. Res., *85,* 3285–3303.

—— 1981. Deep currents and their interpretation as equatorial waves in the western Indian Ocean. J. Phys. Oceanogr., *11,* 48–70.

Hayes, S. P. 1981. Vertical fine structure observations in the eastern equatorial Pacific. J. Geophys. Res., *86(C11),* 10893–10999.

Hayes, S. P. and C. J. Powell. 1980. Vertical wave number spectra of temperature fine structure in the equatorial Pacific. J. Geophys. Res., *85,* 4029–4035.

Leetmaa, A. and P. F. Spain. 1981. Results from a velocity transect along the equator from 125 to 159W. J. Phys. Oceanogr., *11,* 1030–1033.

Lighthill, M. J. 1969. Dynamic response of the Indian Ocean to the onset of the Southwest Monsoon. Phil. Trans. Roc. Soc. London A, *265,* 45–93.

—— 1978. Waves in Fluids, Cambridge University Press, Cambridge, 504 pp.

Lukas, R. B. 1981. The termination of the equatorial undercurrent in the eastern Pacific. Ph.D. thesis, University of Hawaii, 127 pp.

Lukas, R. B. and E. Firing. 1984. An annual Rossby wave in the central equatorial Pacific. J. Phys. Oceanog., (submitted).

Luyten, J. R. 1982. Equatorial current measurements, I. Moored observations. J. Mar. Res., *40,* 19–41.

Luyten, J. R. and D. H. Roemmich. 1982. Equatorial currents at semiannual period in the Indian Ocean. J. Phys. Oceanogr., *12,* 406–413.

Luyten, J. R. and J. C. Swallow. 1976. Equatorial undercurrents. Deep-Sea Res., *23,* 999–1001.

Luyten, J. R., M. Fieux and J. Gonella. 1980. Equatorial currents in the western Indian Ocean. Science, *209,* 600–603.

McCreary, J. P. 1980a. Modelling wind-driven ocean circulation. Tech. Rep. HIG-80-3, Hawaiian Inst. of Geophys., Honolulu, HA 96822, 64 pp.

—— 1980b. A model of the equatorial undercurrent, the coastal undercurrent and deep equatorial jets. Ocean Modelling, *34,* (unpublished manuscript).

—— 1981a. A linear, stratified ocean model of the Equatorial Undercurrent. Phil. Trans. Roy. Soc. London A, *278,* 603–635.

—— 1981b. Modelling deep equatorial jets, *in* Recent progress in equatorial oceanography: a report of the final meeting of SCOR Working Group 47 in Venice, Italy, Fort Lauderdale, Florida: Nova University/NYIT Press, 373–380.

McCreary, J. P., J. Picaut and D. W. Moore. 1984. Effects of remote annual forcing in the eastern tropical Atlantic Ocean. J. Mar. Res., *42,* 45–81.

McPhaden, M. J. 1982. Variability in the central equatorial Indian Ocean Part I: ocean dynamics. J. Mar. Res., *40,* 157–176.

Moore, D. W. 1968. Planetary-gravity waves in an equatorial ocean. Ph.D. thesis, Harvard University.

Moore, D. W. and S. G. H. Philander. 1978. Modelling of the tropical ocean circulation, *in* The Sea, Vol. 6, Wiley-Interscience, New York, 319–361.

Morse, P. M. and H. Feshbach. 1953. Methods of Theoretical Physics, 2 parts, McGraw-Hill, New York.

O'Neill, K. 1982. Observations of vertically propagating equatorially-trapped waves in the deep western Indian Ocean. Tech. Rep. WH01-82-11, Woods Hole Oceanogr. Inst., Woods Hole, MA 02543, 162 pp.

Philander, S. G. H. 1978. Forced ocean waves. Rev. Geophys. Sp. Phys., *16,* 15–46.

Philander, S. G. H. and R. C. Pacanowski. 1981. Response of equatorial oceans to periodic forcing. J. Geophys. Res., *86*(C3), 1903–1916.

Picaut, J., 1983. Propagation of the seasonal upwelling in the eastern equatorial Atlantic. J. Phys. Oceanogr., *13*, 18–37.

Schopf, P. S., D. L. T. Anderson and R. Smith. 1981. Beta-dispersion of low-frequency Rossby waves. Dyn. Atmos. Oceans, *5*, 187–214.

Weisberg, R. H. and A. M. Horigan. 1981. Low-frequency variability in the equatorial Atlantic. J. Phys. Oceanogr., *11*, 913–920.

Wunsch, C. 1977. Response of an equatorial ocean to a periodic monsoon. J. Phys. Oceanogr., *7*, 497–511.

Received: *20 September, 1983;* revised: *24 January, 1984.*